Spin-dependent anisotropic electron-phonon coupling in $KTaO_3$

Giulia Venditti [1], Francesco Macheda [2], Paolo Barone [3], José Lorenzana [4] and Maria N. Gastiasoro [5,*]

[1] *Department of Quantum Matter Physics, University of Geneva, 24 Quai Ernest-Ansermet, 1211 Geneva, Switzerland*

[2] *Dipartimento di Scienze e Metodi dell'Ingegneria, University of Modena and Reggio Emilia, Reggio Emilia, Italy*

[3] *SPIN-CNR Institute for Superconducting and other Innovative Materials and Devices, Area della Ricerca di Tor Vergata, Via del Fosso del Cavaliere 100, 00133 Rome, Italy*

[4] *ISC-CNR Institute for Complex Systems and Department of Physics, Sapienza University of Rome, Piazzale Aldo Moro 2, 00185 Rome, Italy*

[5] *Donostia International Physics Center, 20018 Donostia-San Sebastian, Spain*

(Received 3 November 2025; accepted 28 December 2025; published 26 January 2026)

$KTaO_3$ (KTO) is an incipient ferroelectric, characterized by a softening of the lowest transverse optical (TO) mode with decreasing temperature. Cooper pairing in the recently discovered KTO-based heterostructures has been proposed to be mediated by the soft TO mode. Here, we study the electron coupling to the zone-center odd-parity modes of bulk KTO by means of relativistic Density Functional Perturbation Theory (DFPT). The coupling to the soft TO mode is by far the largest, with comparable contributions from both intraband and interband processes. Remarkably, we find that for this mode, spin nonconserving matrix elements are particularly relevant. We develop a three-band microscopic model with spin-orbit-coupled t_{2g} orbitals that reproduces the main features of the *ab initio* results. For the highest energy band, the coupling can be understood as a "dynamical" isotropic Rashba effect. In contrast, for the two lowest bands, the Rashba-like coupling becomes strongly anisotropic. The DFPT protocol implemented here enables the calculation of the full electron-phonon coupling matrix projected onto any mode of interest, and it is easily applicable to other systems.

DOI: 10.1103/7l88-12m5

I. INTRODUCTION

The anomalous lattice dynamics and dielectric properties of $SrTiO_3$ (STO) and $KTaO_3$ (KTO) have puzzled the condensed matter community for many decades. Their inverse dielectric susceptibility decreases linearly with temperature, extrapolating to a putative Curie temperature at which a transition to a ferroelectric (FE) state should occur. Instead, at low temperatures, the susceptibility saturates and the system remains paraelectric [1,2]. Concomitantly, both STO and KTO show the softening of a transverse optical (TO) mode [3–5] without condensation into the inversion symmetry-breaking FE state. This has been explained in terms of quantum fluctuations, leading to the concept of a quantum paraelectric [6,7], and very recently, in terms of lamellar fluctuations arising from the coupling between the soft TO mode and strain gradients [8].

The introduction of mobile electrons leads to a dilute metallic state with sharp Fermi surfaces (FSs) [9] and interesting physics. Indeed, doped STO was the first material to show a superconducting dome upon doping [10], and despite many decades of research, the superconducting state still defies our understanding [11]. The discovery of gate-tunable superconductivity in STO interfaces and heterostructures with other insulators opened a route to study its two-dimensional limit [12,13]. The presence of a dome and similar transition temperatures $T_c \sim 0.2$ K suggests that they may foster the same pairing mechanism. More recently, a platform for superconductivity was found on the related interfaces between KTO and other oxide insulators, as well as on uncapped KTO surfaces doped with ionic gating [14–22]. The one order of magnitude higher T_c in some of the latest interfaces, up to $\sim$2 K, is not only remarkable but has also the potential to shed light on the pairing mechanism in doped quantum paraelectrics.

The existence of the soft TO mode led to pairing proposals invoking FE fluctuations [23–27], and extensive studies on STO have reported sensitivity of T_c to the putative FE quantum critical point [28–32]. A crucial ingredient in this electron-boson model is the coupling of the itinerant electrons to the soft mode, since transverse modes do not produce long-range electric fields; therefore, the conventional Fröelich electron-phonon coupling vanishes in the infrared limit [33]. Interesting models to overcome this issue have been proposed [11], including a two-phonon coupling [34–37] and a linear Rashba-like electron-phonon coupling (EPC) allowed in the presence of spin-orbit coupling (SOC) [38–42]. The latter has also been discussed in connection with collective modes in the so-called polar metal phase [43], and similar ideas have been invoked in other contexts, such as establishing spin textures by driving coherent phonons [44]. At present, there is no consensus on the mechanism of superconductivity in STO, for either bulk or heterostructures.

The recently discovered interface superconductivity in KTO has the peculiarity of a strong crystallographic

*Contact author: maria.ngastiasoro@dipc.org

orientation dependence of T_c [19], with a maximum for [111] oriented interfaces up to $T_c \approx 2\,\mathrm{K}$ (an order of magnitude higher than in STO), $T_c \approx 1\,\mathrm{K}$ in [110], and $T_c \approx 0.25\,\mathrm{K}$ in [001] [45].

Because of the heavy Ta ion, KTO also presents a strong SOC, splitting the t_{2g} orbitals at Γ by ≈400 meV [46,47], a 14 times larger split than in STO. Moreover, a strong violation of the Pauli limit for in-plane magnetic fields is observed both in [111] and [110] oriented interfaces [48–52], an effect that has been attributed to SOC effects. Interestingly, the softening of the TO mode has also been recently measured in STO- and KTO-based interfaces by surface-sensitive spectroscopy [53]. All these facts raise the question of the relevance of the SOC-assisted Rashba-like coupling to the soft mode for superconductivity and may offer insights into the pairing mechanism.

In the insulating regime, the zero-q longitudinal optical (LO) component stiffens due to the long-range Coulomb interaction, making the soft mode transverse. At low densities, when the electronic plasma frequency is lower than the LO phonon frequency, the LO-TO splitting remains. At sufficiently high densities, however, the electronic screening causes both frequencies to become degenerate, eventually rendering them both soft near the FE instability. In this case, the momentum dependence becomes important, as the screening occurs only for wave vectors smaller than the Thomas-Fermi wave vector. Taking into account the screening of both the matrix elements and the phonon frequency is challenging and requires a very high momentum resolution [54].

Because in the conventional EPC (i.e., without spin-orbit effects), the coupling to the LO phonon dominates, how the LO frequency is treated is crucial. Reference [55] considered both conventional EPC and spin-orbit effects, but, as the authors acknowledge, did not take fully into account the LO-TO splitting. This may lead to overestimating the conventional EPC as the frequency of the LO phonon is assumed to be soft in a large region of momentum space. Hence, it becomes difficult to compare the conventional and SOC-assisted EPC on the same grounds.

Here, we focus on the coupling to the soft mode through the "dynamical" Rashba effect, which is expected to display a weak dependence on momentum and doping, in contrast to the conventional coupling to the LO mode, which requires very demanding numerical resources (i.e., doping-dependent large momentum resolution), beyond our present scope.

The Rashba-like coupling originates from real-space electronic hopping processes induced by the atomic displacements of the phonons. In a simplified model for KTO, they can be understood in terms of hopping processes among spin-1/2 t_{2g} orbitals $|\mu\sigma\rangle$ with $\mu = x, y, z$, corresponding to d_{yz}, d_{zx}, and d_{xy} orbitals, respectively. For *spin-conserving* hopping processes, the EPC matrix element is of order $t_{\mu\nu}$. Here, $t_{\mu\nu}$ is the derivative of a hopping matrix element between two orbitals in neighboring sites with respect to a polar distortion, times the harmonic characteristic length of the phonon, and thus has units of energy. Moreover, SOC itself combined with a lattice distortion can induce *spin nonconserving* hopping processes among t_{2g} orbitals directly or indirectly due to mixing with other orbitals (e.g., via the e_g orbitals of Ta or the p orbitals of O) and orbital polarization effects (e.g., d orbital deforms acquiring f-orbital component). We will refer to these distinct processes as Rashba type I (spin conserving) and Rashba type II (spin nonconserving). We already speculated in Ref. [56] that Rashba-type-II processes may play an important role in the coupling to the soft mode in KTO. In this work, we go beyond the methods in Ref. [56], analyzing type-I and type-II processes on an equal footing.

We study the EPC to the zone-center modes of KTO by comparing relativistic Density Functional Perturbation Theory (DFPT) with a three-band model of spin-orbit-coupled t_{2g} orbitals. Going beyond *frozen-phonon* computations, we compute the total electron-phonon matrix resolved in pseudospin and projected onto KTO zone-center eigenmodes. All modes show comparable contributions from intraband and interband processes, and the coupling to the soft TO mode is found to be the largest. For this mode, Rashba-type-II processes are particularly relevant. The coupling to this mode induces dynamical Rashba-like isotropic chiral angular momentum currents to the highest electronic band. In contrast, for the two lowest bands, the coupling becomes strongly anisotropic, beyond the conventional Rashba effect. The DFPT protocol presented here allows for the extraction of coupling coefficients for a given vibrational eigenvector, including spin effects, and it is easily applicable to other systems.

The paper is organized as follows: in Sec. II, we present the relevant electronic bands and zone-center phonon modes in KTO and introduce the EPC using symmetry arguments; our DFTP protocol and calculations are presented in Sec. III; the three-band microscopic model that reproduces most of the DFPT results is then discussed in Sec. IV, where we demonstrate the importance of spin nonconserving processes in the EPC to the soft mode; and we finally draw our conclusions in Sec. V.

II. ELECTRONS, PHONONS, AND THEIR COUPLING

A. Electronic properties

The electronic structure of KTO near the Fermi level comes mainly from the $5d t_{2g}$ electrons of Ta [57], with a strong SOC splitting of the bands of around 400 meV. In terms of the spinors of the three spin-1/2 t_{2g} orbitals $\varphi^\dagger_\mu(\boldsymbol{k}) = (c^\dagger_{\mu+}(\boldsymbol{k}), c^\dagger_{\mu-}(\boldsymbol{k}))$ (with orbital index $\mu = x, y, z$), the low-energy part of the relativistic *ab initio* electronic dispersion [full lines in Fig. 1(a)] can be described [56] by the following tight-binding (TB) Hamiltonian:

$$\begin{aligned}\mathcal{H}_0 &= \sum_{\boldsymbol{k}}\sum_{\mu\nu} \varphi^\dagger_\mu(\boldsymbol{k}) t^{(0)}_{\mu\nu}(\boldsymbol{k})\sigma_0\varphi_\nu(\boldsymbol{k}) + i\xi[\varphi^\dagger_x(\boldsymbol{k})\sigma_3\varphi_y(\boldsymbol{k}) \\ &\quad + \varphi^\dagger_y(\boldsymbol{k})\sigma_1\varphi_z(\boldsymbol{k}) + \varphi^\dagger_z(\boldsymbol{k})\sigma_2\varphi_x(\boldsymbol{k})] + \mathrm{H.c.}, \qquad (1)\\ &= \sum_{\boldsymbol{k}}\sum_{n} \psi^\dagger_n(\boldsymbol{k})\mathcal{E}_n(\boldsymbol{k})\sigma_0\psi_n(\boldsymbol{k}), \qquad (2)\end{aligned}$$

with the 2×2 identity matrix σ_0, $\boldsymbol{\sigma} \equiv (\sigma_1, \sigma_2, \sigma_3)$, and Pauli matrices σ_i acting on the spinors. Here, $t^{(0)}_{\mu\nu}(\boldsymbol{k})$ are hopping terms between t_{2g} orbitals μ and ν up to next-nearest neighboring Ta atoms, and ξ is the effective atomic SOC (see Appendix A 1 for details). These parameters have been extracted by a fit to the relativistic *ab initio* electronic structure and result in three twofold degenerate electronic bands

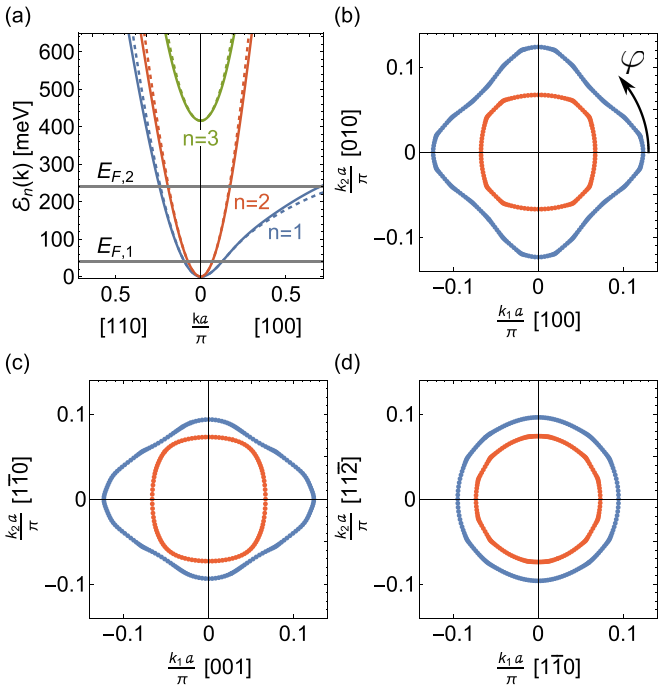

FIG. 1. Electronic band structure of $KTaO_3$. (a) Full lines are the *ab initio* results of the three conduction bands along M-Γ-X. Dashed lines are the tight-binding model [Eq. (1)] with the $3\xi = 416$ meV SOC gap at the zone center. Gray lines are at Fermi energies $E_{F,1} = 40$ meV and $E_{F,2} = 240$ meV. The Fermi surface for $E_{F,1}$ with $n = 1$ outer band (blue) and $n = 2$ inner band (red), in the plane $(k_1, k_2, 0)$ perpendicular to (b) [001], (c) [110], and (d) [111]. The angle in panel (b) is used in Figs. 3, 6, and 7.

$\mathcal{E}_n(\boldsymbol{k})$ [dashed lines in Fig. 1(a)] in terms of the SOC electronic spinors $\psi_n^\dagger(\boldsymbol{k}) = (c_{n+}^\dagger(\boldsymbol{k}), c_{n-}^\dagger(\boldsymbol{k}))$ with pseudospin ±. We will henceforth refer to the doubly degenerate bands as $n = 1, 2, 3$ (blue, red, green).

The transformation from the orbital basis to the band basis is particularly simple close to Γ. Because of the SOC term, at the Γ point states separate into a $j = 3/2$ quartet (bands $n = 1, 2$) and a $j = 1/2$ doublet (band $n = 3$). Here, j is an effective total angular momentum resulting from the mapping of the three t_{2g} orbitals into p orbitals. Then, the effective $l = 1$ orbital angular momentum is added to the spin-1/2 angular momentum [39,41,58,59].

The following states diagonalize the Hamiltonian $\mathcal{H}_0$ up to linear order in momentum around Γ, labeled by the effective total angular momentum and its z projection $\{j, j_z\}$:

$$\begin{aligned}
\left\{\frac{3}{2}, \pm\frac{1}{2}\right\} &: \psi_1^\dagger(\boldsymbol{k}) = \frac{1}{\sqrt{6}}[-i\sigma_2\varphi_x^\dagger(\boldsymbol{k}) - i\sigma_1\varphi_y^\dagger(\boldsymbol{k}) + 2\sigma_0\varphi_z^\dagger(\boldsymbol{k})],\\
\left\{\frac{3}{2}, \mp\frac{3}{2}\right\} &: \psi_2^\dagger(\boldsymbol{k}) = \frac{1}{\sqrt{2}}[i\sigma_2\varphi_x^\dagger(\boldsymbol{k}) - i\sigma_1\varphi_y^\dagger(\boldsymbol{k}))],\\
\left\{\frac{1}{2}, \pm\frac{1}{2}\right\} &: \psi_3^\dagger(\boldsymbol{k}) = \frac{1}{\sqrt{3}}[-i\sigma_2\varphi_x^\dagger(\boldsymbol{k}) - i\sigma_1\varphi_y^\dagger(\boldsymbol{k}) - \sigma_0\varphi_z^\dagger(\boldsymbol{k})].
\end{aligned} \tag{3}$$

Here, the pseudospin index was chosen following the same convention as in Ref. [41]. Note that to linear order in $\boldsymbol{k}$, there is no $\boldsymbol{k}$ dependence of the coefficients of the transformation. As we shall see, the linear order is enough to obtain the behavior of the EPC near Γ.

B. Vibrational properties and electron-phonon coupling

The electron-phonon Hamiltonian to first order in the atomic displacements for the electronic spinor $\psi_n^\dagger(\boldsymbol{k})$ for phonon mode λ is

$$\mathcal{H}_{\mathrm{EPC}} = \frac{1}{\mathcal{N}} \sum_{\boldsymbol{k},nm,\boldsymbol{q}\lambda} \psi_n^\dagger\left(\boldsymbol{k} + \frac{\boldsymbol{q}}{2}\right) \Lambda_{nm,\lambda}(\boldsymbol{k}, \boldsymbol{q}) \psi_m\left(\boldsymbol{k} - \frac{\boldsymbol{q}}{2}\right) \mathcal{A}_{\boldsymbol{q},\lambda}. \tag{4}$$

Here, $\mathcal{A}_{\boldsymbol{q},\lambda} = a_{\boldsymbol{q},\lambda} + a_{-\boldsymbol{q},\lambda}^\dagger$ is the phonon operator, and the general EPC matrix reads

$$\Lambda_{nm,\lambda}(\boldsymbol{k}, \boldsymbol{q}) = g_{nm,\lambda}(\boldsymbol{k}, \boldsymbol{q})\sigma_0 + \boldsymbol{G}_{nm,\lambda}(\boldsymbol{k}, \boldsymbol{q}) \cdot \boldsymbol{\sigma}. \tag{5}$$

The pseudospin-independent coupling $g_{nm,\lambda}(\boldsymbol{k}, \boldsymbol{q})$ is the conventional scalar electron-phonon matrix element. The vector $\boldsymbol{G}_{nm,\lambda}(\boldsymbol{k}, \boldsymbol{q})$ represents instead a pseudospin-dependent coupling, which has been considered less often in literature.

In this work, we will carefully study the intraband ($n = m$) and interband ($n \neq m$) EPC $\Lambda_{nm,\lambda}(\boldsymbol{k}, \boldsymbol{q})$ by a particular postprocessing of electron-phonon coefficients computed with DFPT using Quantum Espresso (QE) in KTO. With respect to our previous work [56], the advantage of DFPT over frozen phonon is twofold: (1) *interband* coupling terms can be accessed, and (2) the computation to any $\boldsymbol{q} \neq 0$ can be straightforwardly extended (without the need of large supercells), which we will also explore.

In cubic KTO, *all* 15 phonon modes at the zone center are odd-parity modes, with irreducible representations (irreps) $4T_{1u} \oplus T_{2u}$. The three acoustic and nine optical (di)polar modes belong to the T_{1u} irrep ($l = 1$), and the three optical octopolar modes to the T_{2u} irrep ($l = 3$). The threefold degeneracy of the irreps corresponds to the three possible polarizations. At infinitesimal $\boldsymbol{q}$, the dipolar triplets get further split by long-range Coulomb into one longitudinal mode and two transverse modes.

In the presence of inversion and time-reversal symmetries, for all these odd-parity zone-center modes the pseudospin-independent intraband term in Eq. (5) must vanish, $g_{nn,\lambda}(\boldsymbol{k}, \boldsymbol{q} = 0)\sigma_0 = 0$, and the pseudospin-dependent term can be finite instead, $\boldsymbol{G}_{nn,\lambda}(\boldsymbol{k}, \boldsymbol{q} = 0) \cdot \boldsymbol{\sigma} \neq 0$ (for the acoustic modes, the coupling is linear in q, so it does trivially vanish at $q = 0$). It would be desirable to obtain the symmetry-allowed form of the nonvanishing intraband coupling $\boldsymbol{G}_{nn,\lambda}(\boldsymbol{k}, \boldsymbol{q} = 0)$ to lowest order in $\boldsymbol{k}$.

The matrix $\boldsymbol{G}_{nn,\lambda}(\boldsymbol{k}, \boldsymbol{q} = 0)$ generally depends on the chosen basis ψ_n. Indeed, because of Kramers degeneracy, any U(2) rotation of the basis produces another allowed basis [60,61]. Near Γ, the basis dependence of the matrix elements can be circumvented by expressing the EPC in terms of matrices representing the effective angular momentum operators $\hat{j}_x$, $\hat{j}_y$, and $\hat{j}_z$.

In the case of $j = 1/2$ [$n = 3$, Eq. (3)], this is particularly simple as the system maps into a spin-1/2 system with angular momentum $\boldsymbol{j}$. In the O_h point group, one can build the following odd-parity objects combining $\boldsymbol{k}$ and $\boldsymbol{j}$: $T_{1u} \otimes T_{1g} = A_{2u} \oplus E_u \oplus T_{1u} \oplus T_{2u}$. From the T_{1u} term, we obtain a

dynamic Rashba-like coupling to polar modes with polarization $\hat{\boldsymbol{n}}$ [26,38,39,62–64],

$$\boldsymbol{G}_{33,T_{1u}^{\lambda}}(\boldsymbol{k},\boldsymbol{q}=\boldsymbol{0})\cdot\boldsymbol{\sigma}=\bar{g}_{3,T_{1u}^{\lambda}}(\hat{k}_x j_y-\hat{k}_y j_x)\hat{n}_z, \tag{6}$$

where the angular momentum matrices j_i are proportional to Pauli matrices. In the presence of a lattice distortion, this form implies a splitting in pseudospin space that is independent of the azimuthal angle φ defined in Fig. 1(b). Here, we have defined the z axis to be parallel to the polarization of the phonon $\hat{\boldsymbol{n}}$, without loss of generality. This coupling is maximum (zero) when the electronic momentum $\boldsymbol{k}$ is perpendicular (parallel) to the polar axis of the mode $\hat{\boldsymbol{n}}$. Analogously, for the T_{2u} term, we obtain a dynamic linear Dresselhaus-like coupling

$$\boldsymbol{G}_{33,T_{2u}}(\boldsymbol{k},\boldsymbol{q}=\boldsymbol{0})\cdot\boldsymbol{\sigma}=\bar{g}_{3,T_{2u}}(\hat{k}_x j_y+\hat{k}_y j_x)\hat{n}_z \tag{7}$$

to octopolar modes.

For the $j=3/2$ manifold, within linear in k order, the degeneracy problem is more severe as the states are fourfold degenerate at Γ and split only quadratically in k by the kinetic energy term in $\mathcal{H}_0$. In contrast, the phonon perturbation produces a linear-in-k splitting. Therefore, in this limit, the phonon-induced mixing between bands $\psi_1^{\dagger}$ and $\psi_2^{\dagger}$ cannot be neglected, and one should consider 4×4 matrices [65,66]. One can show that the $n=1$ intraband term involves $j^{+}=j_x+ij_y$ to the third power and its hermitian conjugate. In general, one can express the perturbation in terms of linear and third powers of $\boldsymbol{j}$ angular momentum matrices. As we shall see, for $j=3/2$, the general form departs from the conventional isotropic Rashba/Dresselhaus forms in that the azimuthal angular dependence of the phonon-induced band splitting becomes important. We call this anisotropic Rashba/Dresselhaus-like EPC [56,57].

In the following, we show how to compute the symmetry-allowed EPC matrix elements for the T_{1u} and T_{2u} modes via relativistic DFPT computations in KTO.

III. DENSITY FUNCTIONAL PERTURBATION THEORY

A. Definitions

We consider the standard Kohn-Sham single-particle Hamiltonian,

$$H=T+V_{\mathrm{KS}}, \tag{8}$$

where T is the noninteracting kinetic energy and V_{KS} is the Kohn-Sham potential containing the Hartree interaction and exchange-correlation effects [67]. The Hamiltonian is diagonalized by the Bloch functions

$$\Psi_{n\eta\boldsymbol{k}}(\boldsymbol{r})=e^{i\boldsymbol{k}\cdot\boldsymbol{r}}u_{n\eta\boldsymbol{k}}(\boldsymbol{r}), \tag{9}$$

where $u_{n\eta\boldsymbol{k}}(\boldsymbol{r})$ have the same periodicity of the lattice and $\eta=\pm$ is the spinor index. We then consider a phonon polarization vector $e^{\lambda}_{\kappa\alpha}(\boldsymbol{q})$, normalized in the unit cell p, for the atom κ along the Cartesian direction α, which induces the following real-space displacement $\boldsymbol{v}$:

$$\upsilon^{\lambda}_{\kappa p,\alpha}(\boldsymbol{q})=e^{\lambda}_{\kappa\alpha}(\boldsymbol{q})e^{i\boldsymbol{q}\cdot(\boldsymbol{R}_p+\boldsymbol{\tau}_\kappa)}, \tag{10}$$

where $\boldsymbol{R}_p$ is the vector that identifies the cell p and $\{\boldsymbol{\tau}_\kappa\}$ are the basis vectors of the atoms κ in the unit cell. Usually, one defines as the electron-phonon coefficients

$$\Lambda_{nm,\lambda}(\boldsymbol{k},\boldsymbol{q})|_{\{\eta,\eta'\}}=\langle u_{n\eta\boldsymbol{k}+\boldsymbol{q}/2}|\Delta_{\boldsymbol{q}\lambda}\upsilon_{\mathrm{KS}}|u_{m\eta'\boldsymbol{k}-\boldsymbol{q}/2}\rangle, \tag{11}$$

where $\Delta_{\boldsymbol{q},\lambda}\upsilon_{\mathrm{KS}}$ is the cell-periodic variation of the Kohn-Sham potential, induced by the displacement of the atom κ along the Cartesian direction α as

$$\Delta_{\boldsymbol{q}\lambda}\upsilon_{\mathrm{KS}}=e^{-i\boldsymbol{q}\cdot\boldsymbol{r}}\Delta_{\boldsymbol{q}\lambda}V_{\mathrm{KS}}, \tag{12}$$

$$\Delta_{\boldsymbol{q}\lambda}\upsilon_{\mathrm{KS}}=\sum_{\kappa\alpha}\sqrt{\frac{\hbar}{2M^{\kappa}\omega_{\boldsymbol{q}\lambda}}}e^{\lambda}_{\kappa\alpha}(\boldsymbol{q})\partial_{\boldsymbol{q}\kappa\alpha}\upsilon_{\mathrm{KS}}, \tag{13}$$

$$\partial_{\boldsymbol{q}\kappa\alpha}\upsilon_{\mathrm{KS}}=\sum_{p}e^{-i\boldsymbol{q}\cdot(\boldsymbol{r}-\boldsymbol{R}_p-\boldsymbol{\tau}_\kappa)}\frac{\partial V_{\mathrm{KS}}}{\partial(R_{p\alpha}+\tau_{\kappa\alpha})}, \tag{14}$$

where M^{κ} is the mass of the atom with $\kappa=\mathrm{Ta},\mathrm{K},\mathrm{O}_x,\mathrm{O}_y,\mathrm{O}_z$. Here, O_μ indicates the three oxygens in the unit cell with identical mass M^{O}.

For the purpose of this work, it is more convenient to compute first the coefficients

$$\gamma^{\kappa\alpha}_{nm}(\boldsymbol{k},\boldsymbol{q})|_{\{\eta,\eta'\}}=\langle u_{n\eta\boldsymbol{k}+\boldsymbol{q}/2}|\partial_{\boldsymbol{q}\kappa\alpha}\upsilon_{\mathrm{KS}}|u_{m\eta'\boldsymbol{k}-\boldsymbol{q}/2}\rangle, \tag{15}$$

which, for a given set of bands n and m, is a 2×2 matrix. Then, we recover the electron-phonon coupling as a 6×6 matrix via

$$\Lambda_{nm,\lambda}(\boldsymbol{k},\boldsymbol{q})=\sum_{\kappa\alpha}\sqrt{\frac{\hbar}{2\omega_{\boldsymbol{q}\lambda}M^{\kappa}}}\gamma^{\kappa\alpha}_{nm}(\boldsymbol{k},\boldsymbol{q})e^{\lambda}_{\kappa\alpha}(\boldsymbol{q}), \tag{16}$$

in terms of phonon eigenvectors $e^{\lambda}_{\kappa\alpha}(\boldsymbol{q})$. In this way, we divide the task of finding the electron-phonon interaction into two subtasks that can be performed independently: (1) compute the matrix elements [Eq. (15)] via DFPT and (2) find, from first principles or experimentally, the phonon eigenvectors and frequencies to insert in Eq. (16).

This procedure guarantees a finer control of the electron-phonon coupling, as one can decide afterward which is the more appropriate phonon eigenvector for a given mode, rather than using the eigenvectors computed by DFPT within the harmonic approximation, as in the standard protocol. This is useful in incipient ferroelectrics, as it may not be *a priori* obvious what phonon eigenvector to use due to intrinsic anharmonicities [68–70]. We present a simple choice below, but our procedure can be generalized to other choices of phonon eigenvectors.

Degeneracies. The electron-phonon coupling of Eq. (16) is expected to contain pseudospin-dependent terms in the form of Eqs. (6) and (7). The *ab initio* $\gamma^{\kappa\alpha}_{nm}$ in Eq. (15) are determined using the ground-state unperturbed Bloch wavefunctions, which present degenerate subspaces $\mathcal{D}_{m\boldsymbol{k}}$ and $\mathcal{D}_{n\boldsymbol{k}+\boldsymbol{q}}$ ($\mathcal{D}_{m\boldsymbol{k}}\geqslant 2$ due to Kramer's theorem and inversion symmetry). This introduces a gauge freedom in the choice of the wavefunctions; therefore, matrix elements in general depend on this choice of gauge. For intraband $\boldsymbol{q}=0$ matrix elements, we can characterize the electron-phonon coupling by reporting the splitting of the band for a given displacement, which is clearly gauge invariant. For all other cases (finite $\boldsymbol{q}$ or interband matrix elements), we will use the gauge-invariant quantity,

$$\mathfrak{g}_{nm,\lambda}(\boldsymbol{k},\boldsymbol{q})=\sqrt{\sum_{\substack{m'\in\mathcal{D}_{m\boldsymbol{k}}\\ n'\in\mathcal{D}_{n\boldsymbol{k}+\boldsymbol{q}}}}\frac{|\Lambda_{n'm',\lambda}(\boldsymbol{k},\boldsymbol{q})|^2}{2}}, \tag{17}$$

for the same purpose.

B. Zone-center modes ($q = 0$)

The atomic displacements of the zone-center optical modes in KTO can be given in terms of a complete set of symmetry coordinates [71] for the T_{1u} ($\bar{S}_1, \bar{S}_2, \bar{S}_3$) and T_{2u} modes ($\bar{S}_4$). In terms of atomic displacements ($s^{\mathrm{K}}, s^{\mathrm{Ta}}, s^{\mathrm{O}_x}, s^{\mathrm{O}_y}, s^{\mathrm{O}_z}$) along [001], they read

$$\bar{S}_1^z = \frac{1}{1+\kappa_1}(0, -\kappa_1, 1, 1, 1), \tag{18}$$

$$\bar{S}_2^z = \frac{1}{1+\kappa_2}(-\kappa_2, 1, 1, 1, 1), \tag{19}$$

$$\bar{S}_3^z = \frac{2}{3}\left(0, 0, -\frac{1}{2}, -\frac{1}{2}, 1\right), \tag{20}$$

$$\bar{S}_4^z = \frac{1}{2}(0, 0, 1, -1, 0), \tag{21}$$

with $\kappa_1 = \frac{3M^{\mathrm{O}}}{M^{\mathrm{Ta}}}$ and $\kappa_2 = \frac{3M^{\mathrm{O}}+M^{\mathrm{Ta}}}{M^{\mathrm{K}}}$. The partners $\bar{S}_\lambda^x, \bar{S}_\lambda^y$ polarized along [100] and [010] are found by the corresponding cyclic operations on atom sites s^{O_i}. From their combination, one can define any mode displacement projected onto the desired direction $\hat{\boldsymbol{n}}$, enforcing the threefold degeneracy of each mode due to the cubic symmetry.

The corresponding eigenvectors are written as

$$e_{\kappa\alpha}^{\lambda}(\boldsymbol{q}=\boldsymbol{0}) \equiv \sqrt{M^\kappa}\eta_{\kappa\alpha}^{\lambda} = \frac{\sqrt{M^\kappa}}{\sqrt{\mu_\lambda}}\bar{S}_\lambda^{\kappa\alpha}\hat{n}_\alpha, \tag{22}$$

with reduced masses

$$(\mu_1)^{-1} = (M^{\mathrm{Ta}})^{-1} + (3M^{\mathrm{O}})^{-1}, \tag{23}$$

$$(\mu_2)^{-1} = (M^{\mathrm{K}})^{-1} + (M^{\mathrm{Ta}} + 3M^{\mathrm{O}})^{-1}, \tag{24}$$

$$(\mu_3)^{-1} = (M^{\mathrm{O}})^{-1} + (2M^{\mathrm{O}})^{-1}, \tag{25}$$

$$(\mu_4)^{-1} = 2(M^{\mathrm{O}})^{-1}, \tag{26}$$

and Eq. (16) becomes

$$\Lambda_{nm,\lambda}(\boldsymbol{k}) = \sum_{\kappa\alpha}\sqrt{\frac{\hbar}{2\omega_{0\lambda}\mu_\lambda}}\gamma_{nm}^{\kappa\alpha}(\boldsymbol{k})\bar{S}_\lambda^{\kappa\alpha}\hat{n}_\alpha. \tag{27}$$

While there is a single possible mode of T_{2u} symmetry ($\bar{S}_4$), the eigenvectors of the three T_{1u} modes in KTO can in principle be any linear combination of $\bar{S}_1, \bar{S}_2$, and $\bar{S}_3$ modes. Experimentally, however, it was established the eigenvectors $\boldsymbol{e}_\kappa^\lambda(\boldsymbol{q}=\boldsymbol{0})$ of the three zone-center T_{1u} modes to be almost pure $\bar{S}_1, \bar{S}_2$, and $\bar{S}_3$ modes, from lowest to highest frequency [68,72,73] (in Appendix B 2, we show that this is the case also from first-principles calculations). That is, the soft TO mode is a nearly "pure" $\bar{S}_1$ mode, with a vibration of the Ta against the oxygen cage. In order to avoid the subtleties involved in a meaningful computation of phonon frequencies and eigenvectors from *ab initio* methods in a system with strong anharmonicities [70] (in particular for modes with a strong temperature dependence, such as the soft TO mode), we will use the *experimental* frequencies and eigenvectors [Eq. (22)] (dressed phonons, instead of the harmonic modes computed within standard DFPT) when computing the EPC [Eq. (27)]. In particular, in the following, we will adopt at $\boldsymbol{q} = \boldsymbol{0}$, $\omega_{01} = 2.5$ meV, $\omega_{02} = 24.7$ meV, and $\omega_{03} = 67.7$ meV, for the $\bar{S}_1, \bar{S}_2$, and $\bar{S}_3$ modes, respectively, and corresponding to the TO modes measured in Refs. [68,73]. As the temperature is raised and the character and frequencies of the phonons get renormalized by anharmonic effects, the EPC can be accordingly modified [Eq. (27)].

We compute Eq. (27) for KTO at the zone center $\boldsymbol{q} = \boldsymbol{0}$, with the computational parameters and procedures listed in Appendix B. Since the zone-center phonons of KTO are odd-parity modes, we do indeed find, in agreement with the symmetry arguments leading to Eqs. (6) and (7), that for intraband processes and $\boldsymbol{q} = \boldsymbol{0}$, the pseudospin-independent processes in Eq. (5) vanish, $g_{nn,\lambda}(\boldsymbol{k})\sigma_0 = 0$.

We can take the 2×2 EPC matrix for each band to be diagonal by transforming to an appropriate basis at each $\boldsymbol{k}$ point. Then, the EPC takes the following pseudospin-dependent form:

$$\Lambda_{nn,\lambda}(\boldsymbol{k}) = \boldsymbol{G}_{nn,\lambda}(\boldsymbol{k})\cdot\boldsymbol{\sigma} = \mathcal{G}_{n,\lambda}(\boldsymbol{k})\sigma_3. \tag{28}$$

Here, for ease of notation, we are using the same symbol $\Lambda_{nn,\lambda}(\boldsymbol{k})$ for the matrix written in the original basis and the matrix in the diagonal basis. Note that the invariant in Eq. (17) is defined so that, for the intraband $n = m$ and $q = 0$ case, it matches $\mathcal{G}_{n,\lambda}(\boldsymbol{k})$ in Eq. (28).

The resulting intraband EPC coupling $\mathcal{G}_{n,\lambda}(\boldsymbol{k})$ for the zone-center modes $\bar{S}_{1,2,3,4}$ polarized along $\hat{\boldsymbol{n}} = [001]$ and for the perpendicular M-Γ-X electronic momentum $\boldsymbol{k}$ path are shown in Fig. 2. In agreement with previous frozen-phonon computations [39,41,56], the EPC is linear in k for $\boldsymbol{k} \to 0$. We have checked that these results are in agreement with frozen-phonon computations with a root mean square error $\lesssim$0.01 meV (see Appendix B 3). As seen, the obtained coupling to the soft $\bar{S}_1$ mode is indeed by far the largest. Also in agreement with Eqs. (6) and (7) for band $n = 3$, the splitting has the same initial slope as a function of the distance from the origin. In contrast, bands $n = 1$ and $n = 2$ show a strong anisotropy of the slope ([100] vs [110]), deviating from the conventional isotropic Rashba splitting.

Because of experimental constraints, the bands $n = 1$ and $n = 2$ are precisely those becoming populated upon doping, as shown in Fig. 1(a) for two illustrative Fermi energies. We are not aware of experiments in which the $n = 3$ band of KTO is populated, either in interfaces or in bulk. Following the strong directional dependence of the superconducting T_c in KTO-based heterostructures, and aiming at a deeper analysis of EPC anisotropies of bands $n = 1$ and $n = 2$ (coalescing to $j = 3/2$ quartet at Γ), we now compute the EPC for three relevant FS cuts, in the planes perpendicular to cubic direction [001], [110], and [111] at $E_{F,1} = 40$ meV, shown in Figs. 1(b)–1(d). We note that these FS cuts cannot be straightforwardly connected to the electronic states at the interfaces: while Ref. [22] reported rough agreement between these cuts and their measurements via soft x-ray angle-resolved photoelectron spectroscopy, significant deviations have been reported at KTO surfaces [74,75], and quantum oscillations [76,77] identify 2D confined nonparabolic subbands coexisting with quasi-three-dimensional (3D) carriers extending deep into KTO. Here, we assume that the soft eigenmode at the surface is still mostly $\bar{S}_1$ [53], and we take the phonon polarization perpendicular to the examined surface. We refer

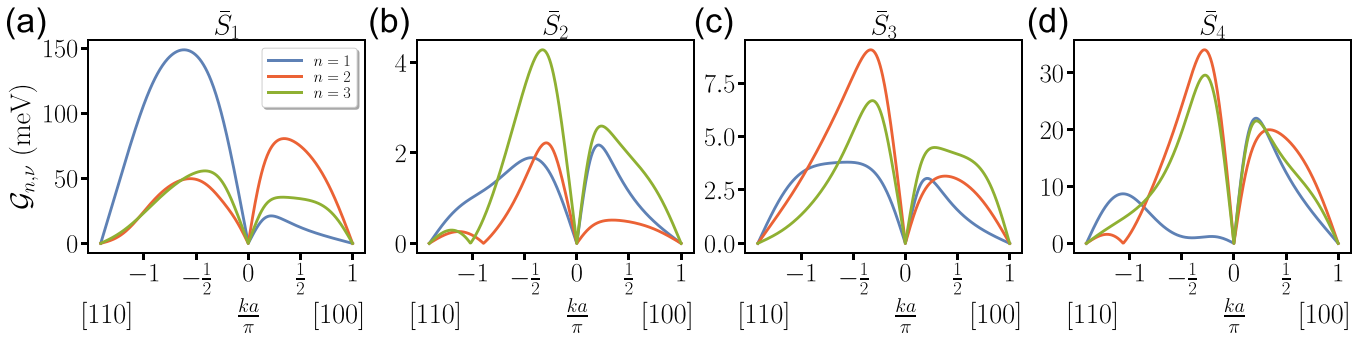

FIG. 2. Intraband EPC to zone-center odd-parity modes polarized along [001] computed by QE. $\mathcal{G}_{n,\lambda}(\boldsymbol{k})$ in Eq. (28) for the electronic band $n=1$ (blue), $n=2$ (red), and $n=3$ (green) for T_{1u} modes (a) $\bar{S}_1$ [Eq. (18)], (b) $\bar{S}_2$ [Eq. (19)], (c) $\bar{S}_3$ [Eq. (20)], and (d) T_{2u} mode $\bar{S}_4$ [Eq. (21)]. The experimental frequencies $\omega_{\boldsymbol{q}=\boldsymbol{0},\lambda}$ have been used in Eq. (27) (Appendix B 2). All modes show linear-in-k EPC around Γ in agreement with Eqs. (6) and (7).

the reader to Appendix B 4 for analogous computations for a phonon polarized parallel to the surface.

Figures 3(a)–3(c) show the intraband EPC for mode $\bar{S}_1$ computed along those three FS orientations, respectively, as the azimuthal angle φ varies along the FS of each band. As seen, the intraband EPC has comparable strength for the three different orientations. However, band structure modifications from 2D confinement effects discussed earlier, and not considered here, could result in strong orientational dependent EPC [19]. This implies that without more detailed computations, no clear clues emerge at this level for the orientational dependence of the T_c on surfaces.

In addition, the EPC shows a rather strong azimuthal angular dependence, also seen in Fig. 2(a) and previous frozen-phonon computations [56]. We anticipate that, when compared to a three-band model (Sec. IV), it will be necessary to consider Rashba-type-II processes (spin nonconserving) to capture the correct angular dependence of the EPC to the Slater $\bar{S}_1$ mode. This was marginally discussed already in Ref. [56], where a frozen-phonon computation along high-symmetry lines was already showing the different anisotropic behavior of the Rashba splitting for the various modes.

A great advantage of DFPT calculations is having access to the interband EPC matrix elements, unlike the frozen-phonon method. In the interband channel, the pseudospin-independent terms $g_{nm,\lambda}(\boldsymbol{k},\boldsymbol{q}=\boldsymbol{0})\sigma_0$ with $n\neq m$ can now also be finite. We indeed find the interband matrices to be of the general form given by Eq. (5). We show in Figs. 3(d)–3(f) the corresponding invariants using Eq. (17) for the lowest bands, $\mathfrak{g}_{12}(\boldsymbol{k})$ and $\mathfrak{g}_{21}(\boldsymbol{k})$, along the FS for the same three orientations [001], [110], and [111], respectively. As seen, these interband matrix elements are of the same order of magnitude as the intraband matrix elements in panels (a)–(c) in the same figure. Since we are considering $\boldsymbol{q}=\boldsymbol{0}$ processes, we show the matrix element for the scattering of a fermion from the FS path of one band to the other band at the same $\boldsymbol{k}$ point, which will be outside the FS. Because of this, the two matrix elements are different ($nm=12$ in blue and $nm=21$ in red).

For completeness, we present the same results for the other two T_{1u} modes, $\bar{S}_2$ and $\bar{S}_3$, and the T_{2u} mode $\bar{S}_4$ in

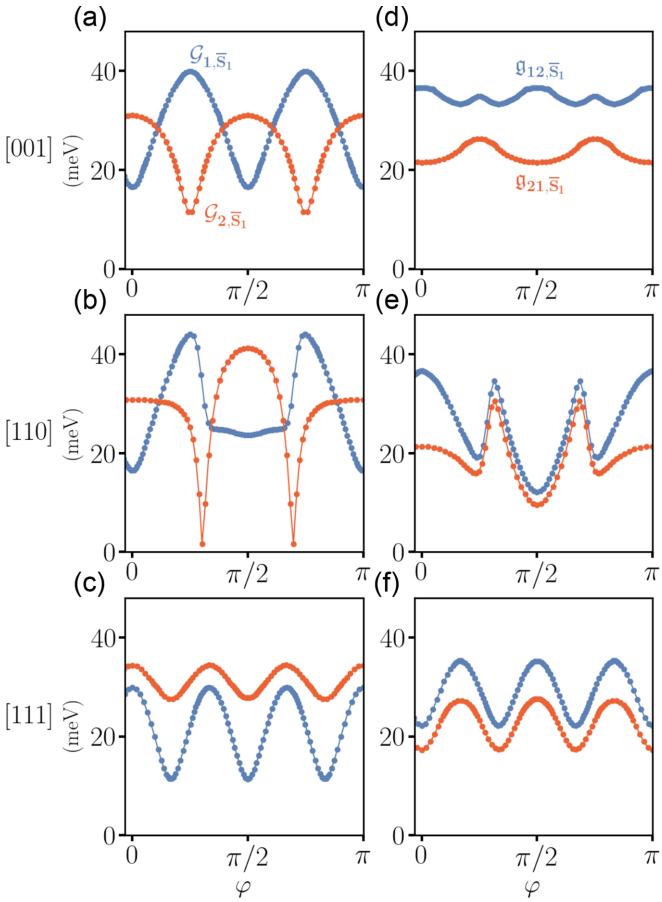

FIG. 3. Orientation dependence of the $\boldsymbol{q}=\boldsymbol{0}$ EPC to the $\bar{S}_1$ mode. Intraband $\mathcal{G}_{n,\bar{S}_1}(\boldsymbol{k},\boldsymbol{q}=\boldsymbol{0})$ along the FS of band $n=1$ (blue) and the FS of band $n=2$ (red) vs azimuthal angle φ [see Fig. 1(b)] in the plane $(k_1,k_2,0)$ perpendicular to (a) [111], (b) [110], and (c) [001]. The Fermi energy is $E_{F,1}=40$ meV and the FSs of the planes are shown in Figs. 1(b) and 1(c). The phonon polarization is perpendicular to the plane examined. The interband matrix elements $\mathfrak{g}_{nm,\bar{S}_1}(\boldsymbol{k},\boldsymbol{q}=\boldsymbol{0})$ with $m\neq n$ for the same orientations are shown in panels (d)–(f). For interband, we show the matrix element for the scattering of a fermion from the FS of one band to the other band at the same $\boldsymbol{k}$ point (since $\boldsymbol{q}=\boldsymbol{0}$), which is outside the FS.

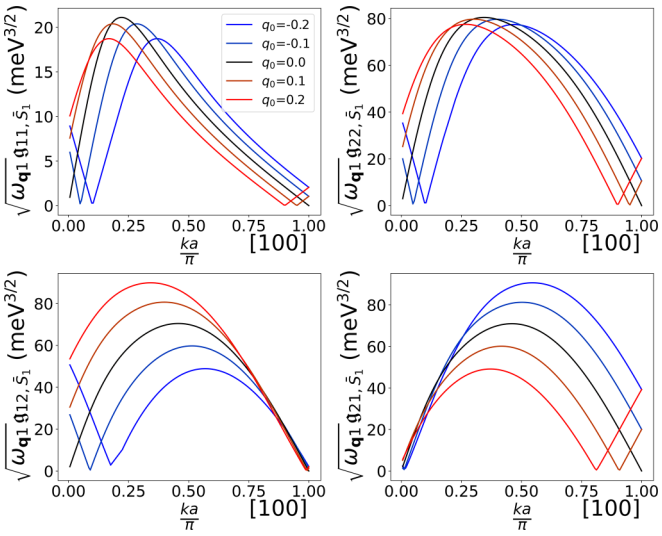

FIG. 4. Intraband $\sqrt{\omega_{\boldsymbol{q}1}}\mathfrak{g}_{11/22,\bar{S}_1}(\boldsymbol{k}+\boldsymbol{q}/2,\boldsymbol{q})$ and interband matrix elements $\sqrt{\omega_{\boldsymbol{q}1}}\mathfrak{g}_{12,1}(\boldsymbol{k}+\boldsymbol{q}/2,\boldsymbol{q})$ using invariant Eq. (17). The polarization of the $\bar{S}_1$ mode is along [001] with $\boldsymbol{k}$ along [100] and $\boldsymbol{q}=(q_0,0,0)$, with $q_0=0,\pm0.1,\pm0.2$ (in units of π/a).

Appendix B 5. Also in this case, despite the strong angular dependence, there is no evident dominance of coupling in any direction.

C. Finite q modes

Within the DFPT framework, it is relatively easy to access electron-phonon matrix elements also at finite $\boldsymbol{q}$. However, differently from the zone-center case, the momentum dependence of the phonon frequency $\omega_{\boldsymbol{q}\lambda}$ and of the phonon eigenvector $e^{\lambda}_{\kappa\alpha}(\boldsymbol{q})$ can in principle have a significant impact on the small-$\boldsymbol{q}$ behavior of $\Lambda_{nm,\lambda}(\boldsymbol{k},\boldsymbol{q})$. Since the experimental determination of the eigenvector of the KTO soft mode at finite $\boldsymbol{q}$ has not been done, we concentrate on the $\boldsymbol{q}$ dependence of the matrix elements $\gamma^{\kappa\alpha}_{nm}(\boldsymbol{k},\boldsymbol{q})$, by computing $\sqrt{\omega_{\boldsymbol{q}\lambda}}\Lambda_{nm,\lambda}(\boldsymbol{k},\boldsymbol{q})$ approximating $e^{\lambda}_{\kappa\alpha}(\boldsymbol{q})$ with the zone-center eigendisplacement of Eq. (22). We show in Fig. 4 these intraband $\sqrt{\omega_{\boldsymbol{q}1}}\mathfrak{g}_{11/22,\bar{S}_1}(\boldsymbol{k}+\boldsymbol{q}/2,\boldsymbol{q})$ and interband $\sqrt{\omega_{\boldsymbol{q}1}}\mathfrak{g}_{12/21,\bar{S}_1}(\boldsymbol{k}+\boldsymbol{q}/2,\boldsymbol{q})$ terms for a $\bar{S}_1$ mode polarized along [001], $\boldsymbol{k}$ along the perpendicular [100] direction, and $\boldsymbol{q}=(q_0,0,0)\parallel\boldsymbol{k}$ with $q_0=0,\pm0.1,\pm0.2$ (in units of π/a).

In general, the presence of a finite $\boldsymbol{q}$ introduces both the dependence of $\gamma^{\kappa\alpha}_{nm}(\boldsymbol{k},\boldsymbol{q})$ upon the angle between $\boldsymbol{k}+\boldsymbol{q}/2$ and $\boldsymbol{k}-\boldsymbol{q}/2$, and on their moduli $|\boldsymbol{k}+\boldsymbol{q}/2|$, $|\boldsymbol{k}-\boldsymbol{q}/2|$. These dependencies shift the minima of $\mathfrak{g}_{nn,\lambda}(\boldsymbol{k}+\boldsymbol{q}/2,\boldsymbol{q})$ away from $\boldsymbol{k}=\boldsymbol{0}$ to $\boldsymbol{k}=-\boldsymbol{q}/2$ at finite $\boldsymbol{q}$, signaling the presence of trigonometric factors. Equivalently, the minima of $\mathfrak{g}_{nn,\lambda}(\boldsymbol{k},\boldsymbol{q})$ always appear at $\boldsymbol{k}=0$ at finite $\boldsymbol{q}$. This is consistent with the fact that in the presence of time-reversal symmetry $|\mathfrak{g}_{nn,\lambda}(\boldsymbol{k},\boldsymbol{q})|=|\mathfrak{g}_{nn,\lambda}(-\boldsymbol{k},\boldsymbol{q})|$ must hold. Additional dependencies on $|\boldsymbol{q}|$ are instead much milder up to the largest $\boldsymbol{q}$ analyzed (Fig. 4). This is probably a general feature of the EPC in this system, but its systematic study will be left for future investigations.

Finally, we note that finite $\boldsymbol{q}$ calculations are continuous to $\boldsymbol{q}=\boldsymbol{0}$ ones, signaling the absence of long-range components in the electron-phonon coupling of the analyzed modes, as expected for TO phonons [54,78,79]. Given the weak $|q|$ dependence found for small doping, it is reasonable to take the $\boldsymbol{q}=\boldsymbol{0}$ results as representative of the interband electron-phonon coupling.

IV. THREE-BAND MODEL OF DYNAMIC RASHBA-LIKE COUPLING

In the following, we show how the EPC to polar modes in Eq. (4) emerges when considering induced electronic hopping processes in real space in a three-band relativistic model with the t_{2g} orbitals of Ta [41]. Indeed, in the presence of a polar distortion, new terms appear in the electronic Hamiltonian. Identifying the dominant ones can help to understand the momentum structure of the EPC (Fig. 3), determine the relevance of spin-conserving (type-I) and spin nonconserving (type-II) processes, and pinpoint the microscopic processes that lead to the symmetry form in Eq. (6).

We now introduce a three-band model (spin-orbit-coupled t_{2g} orbitals) to describe the coupling between the electrons and polar phonons in this system. In the presence of a polar mode λ to linear order in the distortion, there are induced hopping terms $t_{\mu\nu,j,\lambda}(\boldsymbol{k},\boldsymbol{q})$. The EPC Hamiltonian reads

$$\mathcal{H}_{\rm EPC}=\sum_{\boldsymbol{k}\boldsymbol{q},\mu\nu j}\varphi^{\dagger}_{\mu}\Big(\boldsymbol{k}+\frac{\boldsymbol{q}}{2}\Big)t_{\mu\nu,j,\lambda}(\boldsymbol{k},\boldsymbol{q})\sigma_j\varphi_{\nu}\Big(\boldsymbol{k}-\frac{\boldsymbol{q}}{2}\Big)\mathcal{A}_{\boldsymbol{q},\lambda}, \tag{29}$$

with Pauli matrices σ_j representing electronic spin-independent ($j=0$) and spin-dependent ($j=1,2,3$) hopping processes between orbitals μ and ν on neighboring Ta sites.

To identify the most important induced hopping terms, we performed a $\boldsymbol{q}=\boldsymbol{0}$ frozen-phonon computation together with a Wannier projection of the electronic structure with and without the lattice distortion for the three polar modes. We employed maximally localized Wannier functions (MLWFs) [80] with a polar phonon oriented along [001]. The Wannier projection was restricted to the t_{2g} manifold, so all the indirect processes via different orbitals are effectively incorporated in the projection. For further details, see Appendix A 2.

We find strong differences between the odd-parity-induced terms by each polar mode $\bar{S}_{\lambda}$ in KTO. The following four hoppings and their symmetry-related terms between nearest-neighbor (NN) Ta atoms dominate the response:

$$t_{yz,0}(\boldsymbol{k})=-2it_u\sin k_y,\quad t_{zx,0}(\boldsymbol{k})=2it_u\sin k_x, \tag{30}$$

$$t_{xx,1}(\boldsymbol{k})=2\tau_{u,A}\sin k_y,\quad t_{yy,2}(\boldsymbol{k})=-2\tau_{u,A}\sin k_x, \tag{31}$$

$$t_{xy,2}(\boldsymbol{k})=-2\tau_{u,B}\sin k_y,\quad t_{xy,1}(\boldsymbol{k})=2\tau_{u,B}\sin k_x, \tag{32}$$

$$t_{zx,3}(\boldsymbol{k})=-2\tau_{u,C}\sin k_y,\quad t_{yz,3}(\boldsymbol{k})=2\tau_{u,C}\sin k_x. \tag{33}$$

Note that we dropped the $\boldsymbol{q}$ dependence and λ subscript to simplify the notation. The amplitude t_u in Eq. (30) corresponds to the previously studied spin-independent (type-I) process [39,56], and it is shown in Fig. 5(a). The other three terms in Eqs. (31)–(33) correspond to spin-dependent (type-II) processes. The induced term in Eq. (31) is shown in Fig. 5(b) and describes a spin nonconserving intraorbital hopping with amplitude $\tau_{u,A}$. Figure 5(c) describes also a spin nonconserving

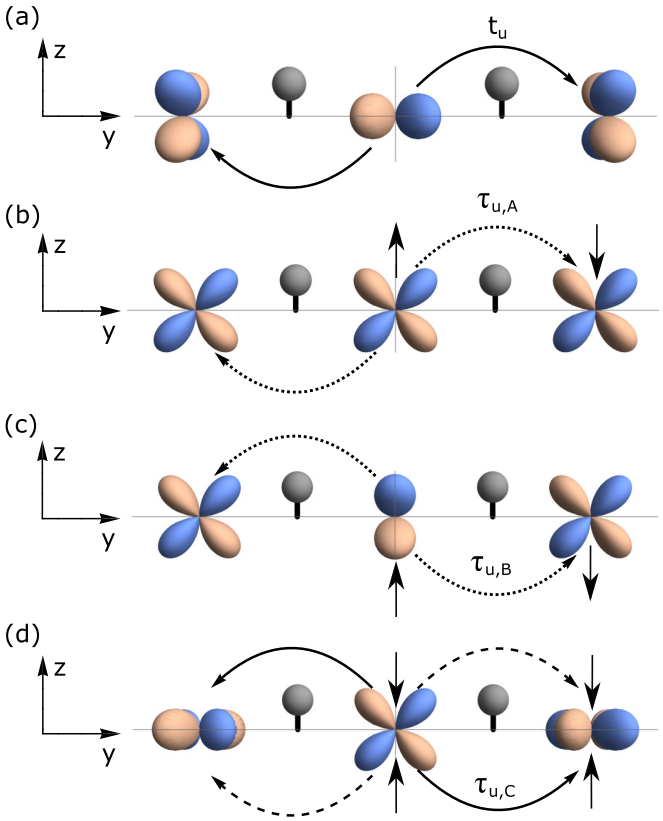

FIG. 5. Schematic induced odd-parity hopping terms in a structure with a polar phonon along $\hat{\boldsymbol{n}} = \hat{z}$. The phonon is represented by the polar displacement of the oxygen atoms (gray spheres) along $\hat{z}$, with induced hopping channels between NN t_{2g} orbitals along the $\hat{y}$ bond. (a) Spin-independent interorbital $t_{yz,0}(\boldsymbol{k})\sigma_0$ [Eq. (30)], (b) spin-flip intraorbital $t_{xx,1}(\boldsymbol{k})\sigma_1$ [Eq. (31)], (c) spin-flip interorbital $t_{xy,2}(\boldsymbol{k})\sigma_2$ [Eq. (32)], and (d) spin-dependent interorbital $t_{zx,3}(\boldsymbol{k})\sigma_3$ [Eq. (33)]. The spin of the orbitals in the relativistic processes is represented by gray arrows, only shown for $y > 0$ for clarity. Notice that the flipping or not of the spin depends on the spin state of the electron considered. We schematically illustrate the processes for spins polarized along the z direction.

term, involving two different t_{2g} orbitals instead [Eq. (32)]. The last type-II term [Eq. (33)] in Fig. 5(d) is an interorbital hopping with spin-dependent amplitude $\tau_{u,C}$, opposite for each spin projection along z. The analogous terms for a polar phonon along [100] and [010] can be straightforwardly derived using a permutation of the orbitals.

Notice that Eqs. (4) and (29) represent the same electron-phonon interaction, the former in the band basis and the latter in the orbital basis. The matrix elements Λ_{nm} and $t_{\mu\nu,j}$ are related by a unitary transformation and are derivatives of an energy with respect to atomic displacements multiplied by the harmonic oscillator characteristic length $l_{\boldsymbol{q}\lambda} \equiv \sqrt{\hbar/(2\omega_{\boldsymbol{q}\lambda}\mu_\lambda)}$ [cf. Eqs. (15) and (27)] and therefore have units of energy. Likewise, the induced hopping parameters have units of energy, and their value depends on the choice of the phonon frequency, while their ratios reported below do not.

Table I shows the ratio of the induced type-II hopping amplitudes $\tau_{u,i}$ to the type-I amplitude t_u for the three polar modes $\bar{S}_\lambda$ in KTO [Eqs. (18)–(20)] obtained from the Wannier

TABLE I. Hopping terms induced by the three polar modes $\bar{S}_i$ in KTO [Eqs. (18)–(20)]. We report the ratio between spin nonconserving (type-II) [Eqs. (31)–(33)] and spin-conserving t_u (type-I) terms [Eq. (30)], obtained from localized Wannier functions. The t_u hopping is obtained from a linear-in-k fit to the EPC obtained in a nonrelativistic DFPT calculation (see Appendix A 3) and using the experimental phonon frequencies listed in Sec. III A.

	$\bar{S}_1$	$\bar{S}_2$	$\bar{S}_3$
$\tau_{u,A}/t_u$	1.08	0.18	−0.35
$\tau_{u,B}/t_u$	0.1	−0.01	0.31
$\tau_{u,C}/t_u$	0.44	0.06	−0.33
t_u (meV)	48.8	4.3	8.3

projection. While the ratios are quite small for the $\bar{S}_2$ mode, they become intermediate for $\bar{S}_3$, and more importantly of the order of 1 for $\bar{S}_1$. This indicates that the spin nonconserving terms in the EPC vertex for the Slater mode $\bar{S}_1$ are as relevant as the spin-conserving interorbital t_u term. This is consistent with the much stronger intraband interaction for all bands in Fig. 2(a) compared to panels (b) and (c), which cannot be reconciled solely with the mode-dependent t_u magnitudes. The magnitude of t_u is discussed in the next subsection, as it was determined by a different method.

We use now the three-band model of t_{2g} orbitals with SOC [Eqs. (1) and (29)] to show how the spin nonconserving terms determine the momentum structure and strength of the polar EPC.

A. Rashba-type-I processes

Let us start by neglecting SOC ($\xi = 0$) in Eq. (1) and doing the analysis for the high-symmetry direction $\hat{\boldsymbol{k}} = [100]$ to obtain analytical expressions. The tight-binding model $\mathcal{H}_0 = \sum_{\boldsymbol{k}} h_0(\boldsymbol{k})$ of the three spin-1/2 t_{2g} orbitals takes the form

$$h_0(\xi = 0, k_x) = \sum_\mu \varphi_\mu^\dagger(k_x) E_\mu(k_x) \sigma_0 \varphi_\mu(k_x), \tag{34}$$

with energy dispersions

$$E_x(k) = 2t_2(1 - \cos k), \tag{35}$$

$$E_y(k) = E_z(k) = 2(t_1 + 2t_3)(1 - \cos k). \tag{36}$$

Again, σ_0 is the identity matrix acting on the electronic spin-$\frac{1}{2}$ sector of the t_{2g} orbitals. Hence, along this $\hat{\boldsymbol{k}} = [100]$ direction, we have a doubly degenerate band with orbital character $\mu = x$ and a fourfold-degenerate band with orbital character $\mu = y, z$. The same holds for the equivalent $\hat{\boldsymbol{k}} = [010]$ direction, but interchanging the x and y orbital character.

Without SOC, a polar phonon can only induce the interorbital spin-independent processes t_u [Eq. (30)]. In the electronic basis φ_μ in Eq. (34), these induced hopping elements for a phonon polarized along [001] become pure *interband* terms, mixing the orbitals $\mu = x, y$ in the lower band with the $\mu = z$ member of the upper band

manifold:

$$\mathcal{H}_{\rm EPC} = \sum_{\boldsymbol{k}} 2it_u[\varphi_x^\dagger(\boldsymbol{k})\sin(k_x)\sigma_0\varphi_z(\boldsymbol{k}) + \varphi_y^\dagger(\boldsymbol{k})\sin(k_y)\sigma_0\varphi_z(\boldsymbol{k})]\mathcal{A}_{q=0} + \text{H.c.} \quad \text{(type I)}. \tag{37}$$

Note that the double spin degeneracy is preserved (the spin sectors up and down are still completely decoupled); i.e., the polar term only acts in the band sector, as an interband spin-conserving coupling.

The t_u parameter could in principle be directly obtained from the relativistic Wannier projection discussed above, which includes this nearest-neighbor hopping amplitude. Instead, we can obtain an *effective* t_u parameter taking into account further Ta neighbors, beyond NN, in the spirit of tight-binding models (for details, see Appendix A 3). We perform a nonrelativistic DFPT computation for a polar mode $\bar{S}_\lambda$. In this case, the second term in Eq. (5) vanishes and Eq. (37) contributes only to the first term, i.e., $\Lambda_{nm,\lambda}(\boldsymbol{k}) = g_{nm,\lambda}(\boldsymbol{k})\sigma_0$ for $n \neq m$. By fitting the DFPT results with the model [Eqs. (34) and (37)], we obtain the effective t_u values in Table I.

The $\bar{S}_2$ mode shows the smallest EPC amplitude, more so when considering $\sqrt{\omega_{0\lambda}}t_u$. This may not be so surprising, since from Eqs. (18)–(20), one can see that this is the only mode preserving the Ta–O bond. We have also checked that in the presence of SOC the t_u parameters from Wannier do not change significantly, the change for the soft $\bar{S}_1$ mode being less than 1%.

Switching on the SOC, we can now project the spin-conserving EPC model [Eq. (37)] into the relativistic electronic spinors $\psi_n^\dagger(\boldsymbol{k})$ in Eq. (2). It is instructive to analyze first the problem in the small k limit, neglecting quadratic and higher order in k corrections, where the electronic basis [Eq. (3)] diagonalizes $\mathcal{H}_0$. Projecting the matrix elements of the type-I EPC model [Eq. (37)] induced by the parity-breaking phonon to the SOC basis in Eq. (3) we obtain

$$\mathcal{H}_{\rm EPC} = \Big[\sum_n \psi_n^\dagger\vartheta_n(k_x\sigma_2 - k_y\sigma_1)\psi_n + \psi_1^\dagger\vartheta_{12}(k_x\sigma_2 + k_y\sigma_1)\psi_2 + \psi_1^\dagger\vartheta_{13}(k_x\sigma_2 - k_y\sigma_1)\psi_3 + \psi_2^\dagger\vartheta_{23}(k_x\sigma_2 + k_y\sigma_1)\psi_3\Big]\mathcal{A}_{q=0} + \text{H.c.}, \tag{38}$$

with the following intraband and interband coupling terms:

$$\vartheta_1 = -\vartheta_3 = -\frac{4}{3}t_u, \tag{39}$$

$$\vartheta_2 = 0, \tag{40}$$

$$\vartheta_{12} = -\sqrt{6}\vartheta_{13} = -\sqrt{2}\vartheta_{23} = \frac{2}{\sqrt{3}}t_u. \tag{41}$$

For band 3, the polar phonon induces a pseudospin-dependent intraband Rashba-like term ϑ_3, recovering the expression in Eq. (6) derived from symmetry arguments for a T_{1u} mode, with coupling constant $\frac{4}{3}t_u$. This leads to the conventional isotropic Rashba splitting in the presence of a static lattice distortion.

A similar result is found for the intraband term of band 1, but, in addition, the phonon also induces pseudospin-dependent ϑ_{nm} interband matrix elements, with a Rashba-like coupling ϑ_{13} and a Dresselhaus-like coupling for ϑ_{12} and ϑ_{23}. Notice that because of the degeneracy of bands 1 and 2 in this k limit, what is called "intraband" and "interband" is basis dependent, and the 4×4 matrix with the interband interaction has to be taken into account to obtain the splitting.

By construction, we considered only type-I processes in Eq. (37). Therefore, all EPC terms in Eqs. (39)–(41) are proportional to the spin-conserving hopping t_u involving interorbital amplitudes [Eq. (30)]. In this case, SOC is only needed to modify the electronic structure (from nonrelativistic to relativistic), but it is not critical for the existence of a finite electron-phonon vertex [39,41,63,81]. In the absence of SOC, the electron-phonon vertex does not vanish but simply becomes a spin-conserving interband term, as in Eq. (37).

From the analytically derived EPC expressions in Eqs. (39)–(41), one can already see that in general the resulting interband ϑ_{nm} and intraband ϑ_n couplings are of the same order of magnitude ($\sim t_u$), in agreement with the *ab initio* results in Fig. 3. One can show analytically, going to quadratic order in k, that the type-I EPC model also displays a vanishing EPC for band $n = 2$ for $k_x = 0$ and $k_y = 0$ [56], which is certainly not the case for the *ab initio* EPC, as can be read from Fig. 2, where the $n = 2$ band shows, at small k, a sizable linear-in-k intraband EPC along k_x for all polar modes.

Interestingly, as we shall see, this model yields an anisotropic Rashba splitting, which is a necessary condition to explain the DFT results. However, the obtained angular dependence is qualitatively different for some of the modes. To illustrate more clearly the problem with neglecting type-II hopping processes in the EPC, Fig. 6 compares the type-I model using Eqs. (1) and (37) (dashed lines in all panels) with relativistic DFPT computations (full lines in all panels) along the same FS $\boldsymbol{k}$ path. That is, projecting $\mathcal{H}_{\rm EPC}$ onto the relativistic electronic basis that diagonalizes $\mathcal{H}_0$ for each $\boldsymbol{k}$ point along the FS of each electronic band n, we get the corresponding EPC matrix $\Lambda_{nm,\lambda}(\boldsymbol{k})$ [Eq. (5)] for a mode λ, from which the intraband (left column) and interband (right column) EPC strengths are obtained and compared to DFPT results. The modes are polarized along $\hat{\boldsymbol{n}} \parallel [001]$, and the EPC is shown as a polar plot, i.e., along the FS of bands $n = 1$ (blue) and $n = 2$ (red) in the perpendicular k_x-k_y plane, for $E_{F,1} = 40$ meV, illustrated in Fig. 1(a). Note that bands 1 and 2 are no longer degenerate [Fig. 1(b)], unlike in the linear-in-k approximation in Eq. (3), due to the mixing by the kinetic energy terms in $\mathcal{H}_0$ at quadratic order in k.

As we already pointed out above and in Ref. [56], the type-I model only captures some of the EPC features obtained by *ab initio* in KTO. As seen in Fig. 6(b), both intraband (left) and interband (right) EPCs of mode $\bar{S}_2$ are beautifully reproduced by this three-band EPC model, both qualitatively and quantitatively. The EPC to the polar mode $\bar{S}_3$ obtained by the model in Fig. 6(c) shows bigger disagreement with its DFPT counterpart, although the general features are still qualitatively captured. Finally, the model severely fails when describing the EPC to the soft mode $\bar{S}_1$, as shown in panel (a). In particular, we highlight the substantial qualitative difference found in the intraband contribution, where the maxima and minima appear inverted for both $n = 1$ and $n = 2$ bands.

The virtue of the type-I EPC model for mode $\bar{S}_2$ and its shortcomings for mode $\bar{S}_1$ (and to some extent $\bar{S}_3$) are not so

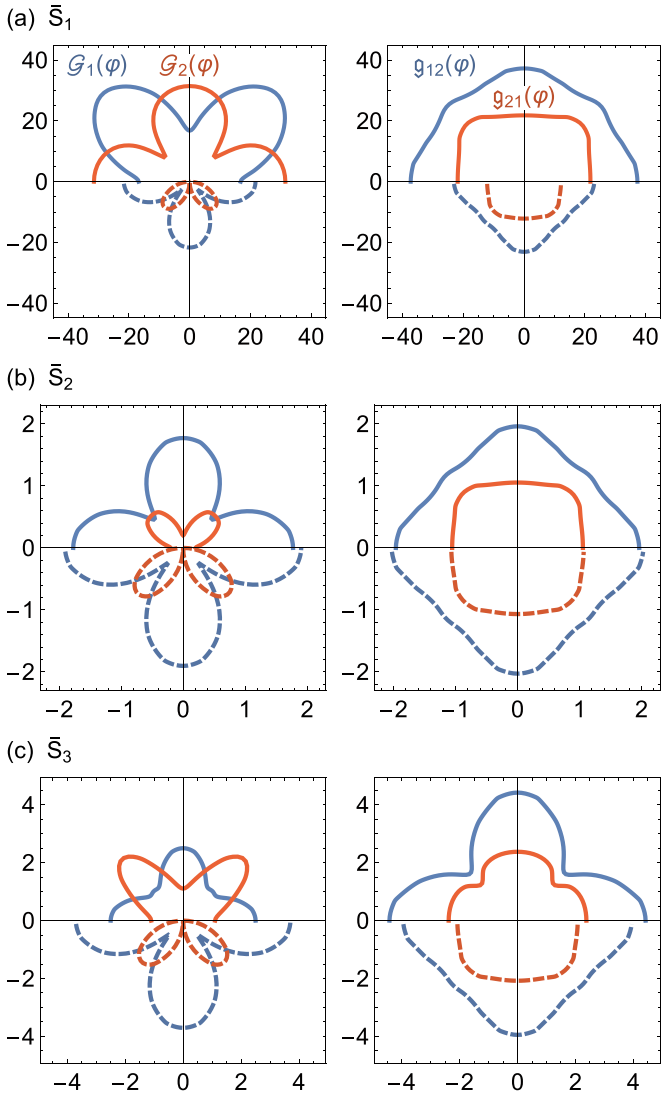

FIG. 6. Type-I EPC model ($\tau_{u,i} = 0$) vs DFPT. Polar plot of the intraband $\mathcal{G}_{n,\lambda}(k_F\varphi)$ (left panels) and interband $\mathfrak{g}_{nm,\lambda}(k_F\varphi)$ (right panels) in millielectronvolts, for a $\boldsymbol{q} = \boldsymbol{0}$ mode λ with polar axis along [001], along the FS of band $n = 1$ (blue), and $n = 2$ (red) in the perpendicular k_x-k_y plane for $E_{F,1} = 40$ meV. In each panel, the EPC is computed both by DFPT (for $0 < \varphi < \pi$, full lines) and by the three-band model in Eqs. (1) and (29), with t_u from Table I (for $-\pi < \varphi < 0$, dashed lines). (a) $\lambda = \bar{S}_1$ [equivalent to Figs. 3(e) and 3(f)], (b) $\lambda = \bar{S}_2$, and (c) $\lambda = \bar{S}_3$.

surprising, if one bears in mind the mode-dependent relevance of the induced spin nonconserving terms $\tau_{u,i}$ discussed in the beginning of this section and listed in Table I. In the following, we show how these type-II terms can considerably affect the EPC structure (and strength) of the three polar modes.

B. Rashba type-I and type-II processes

Let us now consider the EPC model by including also the spin nonconserving terms in Eqs. (31)–(33). We can again project the matrix elements in Eqs. (29)–(33) induced by the polar phonon to the SOC electronic basis [Eq. (3)], as in Eq. (38). The corresponding intraband and interband induced elements, listed in the following, contain now, besides t_u, the spin nonconserving terms $\tau_{u,i}$:

$$\vartheta_1 = -\frac{1}{3}(4t_u - \tau_{u,A} + 2\tau_{u,B} - 4\tau_{u,C}), \tag{42}$$

$$\vartheta_2 = (\tau_{u,A} + 2\tau_{u,B}), \tag{43}$$

$$\vartheta_3 = -\frac{1}{3}(4t_u + 2\tau_{u,A} - 4\tau_{u,B} - 4\tau_{u,C}), \tag{44}$$

$$\vartheta_{12} = \frac{1}{\sqrt{3}}(2t_u + \tau_{u,A} + 2\tau_{u,C}), \tag{45}$$

$$\vartheta_{13} = -\frac{\sqrt{2}}{3}(t_u - \tau_{u,A} + 2\tau_{u,B} - \tau_{u,C}), \tag{46}$$

$$\vartheta_{23} = -\sqrt{\frac{2}{3}}(t_u - \tau_{u,A} + \tau_{u,C}). \tag{47}$$

As seen, the spin-dependent $\tau_{u,i}$ amplitudes also lead to Rashba-like EPC terms at small momenta [e.g., Eqs. (42)–(44)]. Contrary to the type-I Rashba EPC arising from the spin-independent t_u amplitude explored before, $\tau_{u,i}$ are proportional to SOC (they must vanish without relativistic effects). We thus call the type of EPC originating from $\tau_{u,i}$ spin-dependent vertex, *Rashba type-II* EPC.

It is interesting to note that the induced terms t_u, $\tau_{u,A}$, $\tau_{u,B}$, and $\tau_{u,C}$ [Eqs. (30)–(33)] enter the intraband ϑ_n and interband ϑ_{nm} EPC of the various bands in distinct ways. For example, the coupling for band $n = 2$ [Eq. (43)] has only spin nonconserving contributions $\tau_{u,i}$, while bands $n = 1, 3$ have contributions from the spin-conserving t_u term as well. This already indicates that the relative strength of the induced type-II terms $\tau_{u,i}$ with respect to the type-I term t_u for a given polar mode determines the final momentum structure of the EPC.

The dashed lines in all panels of Fig. 7 show the intraband (left) and interband (right) EPC by the type-I and type-II model, i.e., using Eqs. (1) and (29) with the induced t_u and $\tau_{u,i}$ parameters in Table I for each $\bar{S}_i$ polar mode, along the same FS $\boldsymbol{k}$ path used in the DFPT calculations (full lines in the same figure). As seen, overall the qualitative match between the three-band model and the *ab initio* results is now very good also for modes $\bar{S}_1$ and $\bar{S}_3$, in particular for the interband matrix elements. Also, it is clear that the different weight of the type-II-induced terms in each polar mode (Table I) affects both the overall EPC strength (e.g., $\bar{S}_1$ vs $\bar{S}_3$, despite having similar $t_u\sqrt{\omega_\lambda}$) as well as the EPC momentum structure (e.g., $\bar{S}_1$ vs $\bar{S}_{2,3}$).

A strength of this framework is that, being a lattice model, it is not restricted to the small-k regime. We show in Fig. 8(a) the comparison between DFPT and the EPC of the three-band model for a high $E_{F,2} = 240$ meV case [indicated also in Fig. 1(a)]. As seen, even when parts of the FS extend close to the Brillouin zone edge (along the [100] and symmetry equivalent directions) the agreement between the EPC by the three-band model (dashed lines) and *ab initio* computations is very good.

As a consequence, another notable strength of the EPC model [Eq. (29)] is that one can straightforwardly map out the 3D $\boldsymbol{k}$-space EPC, bypassing the computational effort required by relativistic DFPT and similar *ab initio* methods.

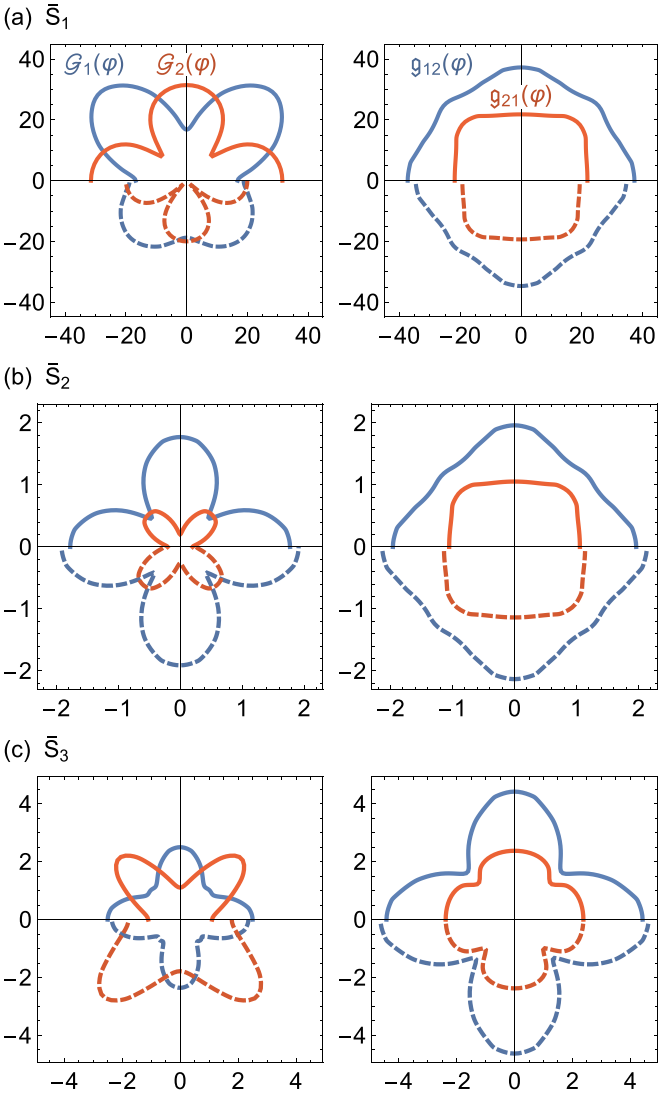

FIG. 7. Type-I and type-II EPC model ($\tau_{u,i} \neq 0$) vs DFPT. Polar plot of the intraband $\mathcal{G}_{n,\lambda}(k_F\varphi)$ (left panels) and interband $\mathfrak{g}_{nm,\lambda}(k_F\varphi)$ (right panels) in millielectronvolts, for a $\boldsymbol{q} = \boldsymbol{0}$ mode λ with polar axis along [001], along the FS of band $n = 1$ (blue), and $n = 2$ (red) in the perpendicular k_x-k_y plane for $E_{F,1} = 40$ meV. In each panel, the EPC is computed both by DFPT (for $0 < \varphi < \pi$, full lines) and by the three-band model in Eqs. (1) and (29) with t_u and $\tau_{u,i}$ from Table I (for $-\pi < \varphi < 0$, dashed lines). (a) $\lambda = \bar{S}_1$ [equivalent to Figs. 3(e) and 3(f)], (b) $\lambda = \bar{S}_2$, and (c) $\lambda = \bar{S}_3$.

Figures 8(b) and 8(c) show an example of the EPC projected on the 3D FSs for $E_{F,1} = 40$ meV and $E_{F,2} = 240$ meV, respectively, for a $\bar{S}_1$ mode polarized along [001] (black arrow). The corresponding 2D cuts on the $k_z = 0$ plane were shown in Figs. 7(a) and 8(a). As seen, the FS acquires anisotropy in momentum space as E_F is increased, from the quasisphere shape in panel (b) to the three interpenetrating ellipsoids oriented along [100], [010], and [001] in panel (c). The structure of the EPC evolves accordingly, showing very large anisotropy in panel (c), with stronger (weaker) coupling in areas close to (far from) the zone center, where the effect of SOC (kinetic term) dominates [41]. These types of 3D maps can be used to

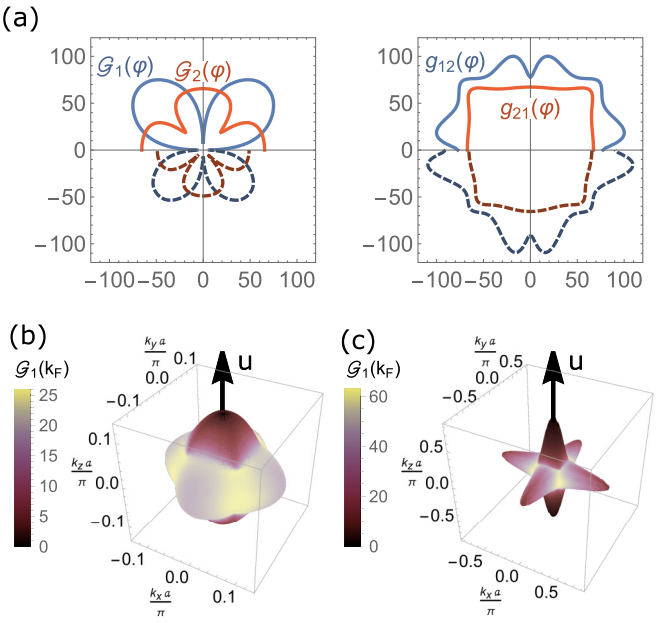

FIG. 8. Three-band model beyond small k and on 3D FSs. (a) Same as Fig. 7(a) but for higher Fermi energy $E_{F,2} = 240$ meV [shown in Fig. 1(a)]. (b) Intraband EPC $\mathcal{G}_{1,\bar{S}_1}(k_F\hat{\boldsymbol{k}})$ for a $\bar{S}_1$ mode polarized along [001] (black arrow), projected on the 3D FS for $E_{F,1} = 40$ meV and (c) $E_{F,2} = 240$ meV. Obtained by the three-band model in Eqs. (1) and (29) with parameters from Table I. The units are millielectronvolts.

study phenomena where the EPC may play an important role, such as transport, superconductivity, or ferroelectric states.

V. SUMMARY AND CONCLUSIONS

We have studied the EPC to the zone-center phonons in KTO, which are odd-parity modes. We focused mainly on the polar T_{1u} modes, particularly on the soft TO mode, employing a combination of relativistic DFPT and a three-band microscopic model. Our computations go beyond the *frozen-phonon* method, where only intraband terms can be studied, and we find that interband matrix elements are of the same order of magnitude as intraband elements. Therefore, interband terms cannot be *a priori* neglected when addressing KTO, and its importance in a physical process must be assessed on a case-by-case basis.

The DFPT results can be understood in terms of a three-band model for the spin-orbit-coupled t_{2g} orbitals. After projecting onto the relevant modes, we can study intraband and interband EPC and disentangle spin-conserving type-I and spin nonconserving type-II processes. The spin-orbit-assisted EPC results to be an isotropic dynamical Rashba effect for band 3 ($j = \frac{1}{2}$) and an anisotropic one for bands 1 and 2 ($j = \frac{3}{2}$).

We find that, for the soft TO mode ($\bar{S}_1$), spin nonconserving hopping terms are as large as spin-conserving terms ($\tau_{u,A} = 1.08\,t_u$, $\tau_{u,C} = 0.44\,t_u$) and need to be included to obtain the correct form of the anisotropy of the EPC in this system. Therefore, SOC is important not only in the mixing of orbitals for the electronic band structure, but also in determining their

coupling to the phonon modes. The match between the three-band model and DFPT results is very good for all three modes, particularly for interband matrix elements. The discrepancy found for intraband matrix elements is largest in the EPC of modes with significant spin nonconserving processes $\bar{S}_1$ and $\bar{S}_3$ [Figs. 7(a) and 7(c)]. Since the origin of these terms is relativistic, it could be due to restricting the model to the t_{2g} manifold, and an obvious extension would be to include the e_g manifold. Another possibility would involve subleading terms beyond neighboring Ta sites in Eqs. (30)–(33), which, according to the Wannier projection, are individually smaller, but their cumulative role could be quantitatively appreciable.

The three-band model works surprisingly well also beyond small $\boldsymbol{k}$. As such, it also allows for a 3D map of the $\boldsymbol{k}$-space EPC, which can be useful for the study of phenomena involving EPC, such as transport, superconductivity, or ferroelectricity. Indeed, we find the coupling to the soft TO mode to be rather large, making the Rashba-like coupling a promising pairing mechanism in KTO. The role of interband coupling in the Cooper channel should be considered in this case. We also note the EPC values obtained by DFPT are significantly larger than the estimate of Ref. [19]. It would be interesting to explore the effect these larger values and the inclusion of spin nonconserving terms have on the resulting pairing coupling constant and gap anisotropy of bilayer models.

The electron-phonon coupling projected on FS cuts perpendicular to different crystallographic orientations shows anisotropies. However, we did not find an evident dominant feature that could explain the different behavior of sample interface orientation regarding superconductivity. That said, one should take into account that a small change in the EPC can be strongly amplified due to the exponential dependence of T_c on the EPC at weak coupling. 2D confinement effects and subbands, not considered here, can also result in orientational dependent EPC [19]. Therefore, the explanation of the observed anisotropy on T_c requires detailed computations on the interface that go beyond our present scope. One step in this direction would be to consider surface and interface phonons [53,82].

Our DFPT protocol was built to be general and allow for the extraction of model coefficients for a given phonon mode. By computing, in fact, the first-order coefficients of the Kohn-Sham Hamiltonian for each atom and direction, we can project them onto the appropriate mode basis. This circumvents the eventual numerical problems arising when computing degenerate phonon modes, which will be, in general, a mixture of the $\bar{S}_\lambda$ modes. This method is quite general and may be applied to any other system with even or odd-parity vibrational modes.

ACKNOWLEDGMENTS

We thank I. Paul, D. Pelc, and M. R. Norman for fruitful discussions. M.N.G. was supported by the Grants No. RYC2021-031639-I and No. PID2023-153277NB-I00 funded by MCIN/AEI/10.13039/501100011033. G.V. acknowledges support from the Swiss National Science Foundation (SNSF) via Swiss Postdoctoral Fellowship Grant No. TMPFP2 224637. We acknowledge the CINECA award under the ISCRA initiative Grants No. HP10CPHFAR and No. HP10CMZFMM, for the availability of high-performance computing resources and support.

DATA AVAILABILITY

The data that support the findings of this article are openly available [83].

APPENDIX A: DETAILS OF THE THREE-BAND MODEL

1. Parameters for electronic bands

We include hopping terms up to next-nearest neighboring t_{2g} orbitals in Ta atoms for the tight-binding model in Eq. (1),

$$t^{(0)}_{\mu\mu}(\boldsymbol{k}) = -2t_1(\cos k_\alpha + \cos k_\beta) - 2t_2 \cos k_\mu - 4t_3 \cos k_\alpha \cos k_\beta + (4t_1 + 2t_2 + 4t_3), \quad \text{(A1)}$$

$$t^{(0)}_{\mu\nu}(\boldsymbol{k}) = -4t_4 \sin k_\mu \sin k_\nu, \quad \text{(A2)}$$

with parameters $t_1 = 483.9\,\text{meV}$, $t_2 = 30.36\,\text{meV}$, $t_3 = 196.9\,\text{meV}$, and $t_4 = 27.6\,\text{meV}$ obtained by fitting the QE electronic structure [Fig. 1(a)]. In Eq. (A1), $\alpha \neq \beta \neq \mu$, while in Eq. (A2), $\mu \neq \nu$. The SOC gap at the zone center in Fig. 1(a) is given by $3\xi = 415.9\,\text{meV}$. The parameters are overall consistent with those given in Ref. [56], whereas the small differences can be ascribed to the slightly larger lattice constant adopted here as well as to different implementations of DFT in QE (used in this paper) and VASP (used in Ref. [56]).

2. Wannierization

We projected the fully relativistic band structure of KTO on MLWFs [80] as implemented in WANNIER90 [84]. Conduction bands of cubic KTO calculated with QE have been projected on spinor Wannier functions localized on Ta atoms with real angular functions yz, xz, and xy, corresponding to spin-1/2 t_{2g} orbitals $|\mu\sigma\rangle$ introduced before, with $\mu = x, y, z$, respectively. FS cuts have been then calculated using the Wannier interpolation procedure implemented in WANNIER90 [80,84] along three different slices in the Brillouin zone, perpendicular to [001], [110], and [111] directions; each slide has been sampled on a uniform 100×100 k-point grid for two values of the Fermi energy ($E_{F,1} = 40\,\text{meV}$ and $E_{F,2} = 240\,\text{meV}$) defined from the conduction band minimum.

We also construct a real-space TB Hamiltonian in the basis of MLWFs (MLWF-TB), which automatically includes also terms beyond next-nearest neighbors. Since indirect processes via different orbitals/atoms are effectively included when downfolded to the t_{2g} manifold, SOC effects are accounted for by both a local term (effective atomic SOC) and by complex hopping interactions. SOC-induced effective parameters can be identified by comparing the MLWF-TB Hamiltonians constructed from *ab initio* calculations with and without SOC. The local SOC has the form given in Eq. (1) with a coupling constant $\xi_{\text{MLWF}} = 139.2\,\text{meV}$, while SOC-induced hopping terms are on the order of a few millielectronvolts and can be thought of as being effectively absorbed in the effective SOC of the three-band tight-binding model [Eq. (1)]. For completeness, we also provide the TB-MLWF parameters up to next-nearest neighbors, $t_1^{\text{MLWF}} = 473.1\,\text{meV}$, $t_2^{\text{MLWF}} = 23.2\,\text{meV}$, $t_3^{\text{MLWF}} = 81.5\,\text{meV}$, and $t_4^{\text{MLWF}} = 13.8\,\text{meV}$. It is

worth mentioning that the TB-MLWF Hamiltonian includes hopping terms beyond next-nearest neighbors, which can be thought to be effectively absorbed in the three-band TB model of Eq. (1), explaining the different values of TB parameters.

The identification of induced hopping terms arising from polar phonons has been achieved within a $\boldsymbol{q} = \boldsymbol{0}$ frozen-phonon approach. We constructed three distorted structures following the $\bar{S}_\lambda$ modes along the [001] direction with fixed amplitude $u = 0.002$ Å to guarantee linearity of the coupling to polar modes [56]. The band structure with and without SOC of each distorted cell has been projected on Ta t_{2g} MLWFs. By analyzing the computed MLWF-TB Hamiltonians, we can single out the odd-parity hopping interactions induced by the lowering of symmetry, as well as their nonrelativistic or relativistic origins. Such frozen-phonon-induced hopping parameters $\bar{t}_{\mu\nu,\sigma\sigma'}$ can be related to the EPC entering in Eq. (29) exploiting the linearity of the coupling regime, hence by multiplying $\bar{t}_{\mu\nu,\sigma\sigma'}$ with the ratio $l_{\boldsymbol{q}=\boldsymbol{0},\lambda}/u$.

When SOC is turned off, the largest induced hopping for the Slater $\bar{S}_1$ mode is the nearest-neighbor one, giving rise to type-I EPC parametrized by t_u. We find that next-nearest-neighbor processes also contribute to type-I EPC: Such contributions are subdominant for the $\bar{S}_1$ mode, while for $\bar{S}_2$ and $\bar{S}_3$ modes they are comparable in strength with the NN process. The type-I EPC parameters evaluated from nonrelativistic MLWFs, but taking into account only the nearest-neighbor contribution, are $t_u(\bar{S}_1) = 35.9$ meV, $t_u(\bar{S}_2) = 1.7$ meV, and $t_u(\bar{S}_3) = 2.6$ meV. Remarkably, they display the same order of magnitude of type-I EPC effective parameters t_u evaluated by fitting nonrelativistic DFPT results with the model [Eq. (37)] (thus taking into account beyond-NN contributions) and listed in Table I. By including contributions arising from next-nearest-neighbor-induced hoppings in the TB-MLWF Hamiltonian, the type-I EPC parameters are modified as $t_u(\bar{S}_1) = 48.9$ meV, $t_u(\bar{S}_2) = 2.8$ meV, and $t_u(\bar{S}_3) = 3.9$ meV. Finally, the inclusion of SOC introduces subleading modifications to the type-I spin-conserving term, namely, $t_u(\bar{S}_1) = 36.1$ meV, $t_u(\bar{S}_2) = 1.7$ meV, and $t_u(\bar{S}_3) = 2.8$ meV, when considering NN hoppings. At the same time, several odd-parity spin-dependent hopping terms mediated by SOC appear in the distorted structures.

In order to keep the TB modelization as simple as possible, while still capturing the essential physics qualitatively, we singled out the leading spin-dependent hopping processes between nearest neighbors that are sketched in Fig. 5. They can be interpreted as arising from indirect processes involving spin-orbit-coupled different orbitals/atoms that are downfolded into the spin-1/2 t_{2g}-only manifold. For instance, the process sketched in Fig. 5(b) between two Ta atoms across a bridging O atom in the Ta^L-O-Ta^R bond may arise from SOC mixing O-p states with opposite spin via the sequence $d^L_{yz,\uparrow} \xrightarrow[\text{i-hop}]{} p_{y,\uparrow} \xrightarrow[L_xS_x]{} p_{z,\downarrow} \xrightarrow[\text{hop}]{} d^R_{yz,\downarrow}$, where we label i-hop and hop the hopping processes between Ta-d and O-p states induced or not by the polar distortion. An alternative indirect process contributing to the same effective matrix element but involving Ta-e_g states can occur along the sequence $d^L_{yz,\uparrow} \xrightarrow[\text{i-hop}]{} p_{y,\uparrow} \xrightarrow[\text{hop}]{} d^R_{x^2-y^2,\uparrow} \xrightarrow[L_xS_x]{} d^R_{yz,\downarrow}$. We notice that the importance of analogous indirect processes has been already emphasized when analyzing the "static" Rashba effect arising from structural inversion symmetry in the two-dimensional electron gas that emerges at perovskite oxide surfaces [85–87], at interfaces in oxide heterostructures [88,89] or in layered perovskites [90]. Due to the large atomic SOC of 5d transition metals such as Ta, indirect processes involving e_g states have been suggested as the dominant contribution to the effective hoppings between t_{2g} orbitals induced by the inversion symmetry breaking [88,90]. The leading effective spin-dependent hopping processes induced by the three polar modes are parametrized by three independent coefficients $\tau_{u,A}$, $\tau_{u,B}$, $\tau_{u,C}$ for each mode, listed in Table I and given in units of the spin-independent-induced hopping t_u.

3. Extract type-I parameter from nonrelativistic DFPT

We can do the same analysis as in Sec. IV A but for $\boldsymbol{k}$ along [110]. In this case, the three-band hopping Hamiltonian reads

$$h_0(\xi = 0, \boldsymbol{k}_M) = \sum_{i=1,2,3} \varphi_i^\dagger(\boldsymbol{k}_M) E_i(\boldsymbol{k}_M) \sigma_0 \varphi_i(\boldsymbol{k}_M), \tag{A3}$$

with energy dispersions

$$\begin{aligned} E_1(\boldsymbol{k}_M) &= 4\left[t_1 + 2t_3 + t_2 - 2t_4\left(1 - \cos\frac{k}{\sqrt{2}}\right)\right]\sin^2\frac{k}{2\sqrt{2}}, \\ E_2(\boldsymbol{k}_M) &= 4[t_1 + 2t_3 + t_2 + 2t_4(1 - \cos k)]\sin^2\frac{k}{2\sqrt{2}}, \\ E_3(\boldsymbol{k}_M) &= 8\left[t_1 + t_3\left(1 + \cos\frac{k}{\sqrt{2}}\right)\right]\sin^2\frac{k}{2\sqrt{2}}. \end{aligned} \tag{A4}$$

Along this $\boldsymbol{k}$ direction, we have three doubly spin-degenerate bands. Considering the same spin-independent interorbital matrix elements induced in the presence of a polar phonon, we obtain again pure *interband* terms for the type-I model:

$$\begin{aligned} h_{\mathrm{EPC}}(\boldsymbol{k}_M) &= \left[-2it_u\sqrt{2}\sin\left(\frac{k}{\sqrt{2}}\right)\varphi_1^\dagger(\boldsymbol{k}_M)\sigma_0\varphi_3(\boldsymbol{k}_M)\right]\mathcal{A}_{q=0} \\ &\quad + \mathrm{H.c.} = \varphi_1^\dagger(\boldsymbol{k}_M)\Lambda_{13}(\boldsymbol{k}_M)\varphi_3(\boldsymbol{k}_M)\mathcal{A}_{q=0} + \mathrm{H.c.}, \end{aligned} \tag{A5}$$

which is analogous to the result in Eq. (37), i.e., interband hopping terms that preserve spin degeneracy.

Doing a nonrelativistic DFPT computation in KTO for a polar $\bar{S}_i$ mode ($i = 1, 2, 3$) polarized along 001, we indeed obtain interband terms along $\boldsymbol{k} = \boldsymbol{k}_X$ and $\boldsymbol{k} = \boldsymbol{k}_M$ within DFPT, shown in Fig. 9 (orange line) for the three polar $\bar{S}_i$ modes. From the fit of these results at small k with Eqs. (37) and (A5), we extract the type-I-induced amplitude t_u for each mode, listed in Table I.

APPENDIX B: COMPUTATIONAL DETAILS

1. Density functional theory calculations

We first computed the optimum value of the cell parameter a of KTO. In Fig. 10, we show the computed total energy E_{tot} of KTO as a function of volume $V = a^3$ (left axis, black) and the corresponding computed pressures P (right axis, red). We fitted the curve $E_{\mathrm{tot}}$with the Birch-Murnaghan potential [91] and P with its derivative. We then took the cell parameter corresponding to zero pressure, indicated by $a_{P=0}$

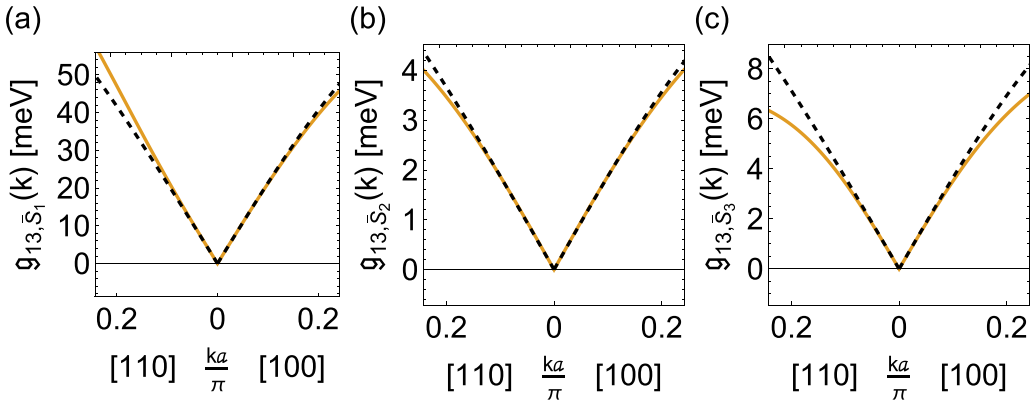

FIG. 9. EPC interband term from nonrelativistic DFPT computation along high-symmetry direction (orange lines) for polar modes (a) $\bar{S}_1$, (b) $\bar{S}_2$, and (c) $\bar{S}_3$ polarized along [001]. Fitting the small k region to Eqs. (37) and (A5) (black dashed lines), we obtain the value for t_u, listed in Table I.

in the plot. We found $a_{P=0} = 1.007\, a_{\text{exp}} = 4.0175$ Å (green stars), where $a_{\text{exp}} = 3.9885$ Å is the experimental value [92]. This relaxation procedure was done using an automatic mesh $10 \times 10 \times 10$, checking that the results for $a_{P=0}$ were unchanged using a tighter grid of $14 \times 14 \times 14$. In both cases, E_{tot} remained the same up to the sixth digit (in Ry units) and the pressure computed in QE at $a_{P=0}$ was found to be $P = 0.56$ kbar, low enough to have a reliable convergence in optical phonons. In all our calculations, we then used $a_{P=0}$ as the cubic cell parameter and an automatic mesh $10 \times 10 \times 10$ for the self-consistent calculations.

To further ease the calculations, we give as input in the self-consistent QE calculation the 56 k points with the correct weights corresponding to the automatic $10 \times 10 \times 10$ automatic grid, plus the k path (with zero weight) along which we want to compute the EPC: High-symmetry lines M-Γ-X are given with a total of 400 equidistant points; FSs are instead computed via the Wannier interpolation procedure explained in Appendix A 2.

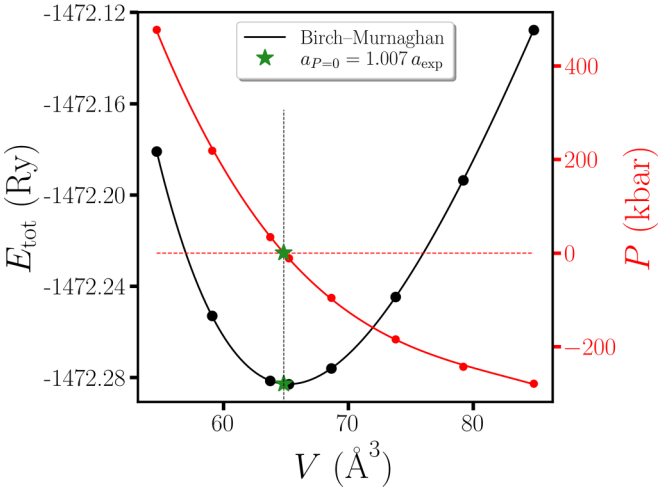

FIG. 10. Relaxation cell procedure. Total energy E_{tot} computed within the QE self-consistent calculation as a function of volume $V = a^3$ (left axis) and corresponding pressure P (right axis, red). Solid lines are the Birch-Murnaghan energy potential fit of E_{tot} (black) and its derivative (P, red). We take the value $a_{P=0} = 1.007\, a_{\text{exp}}$ (green stars), corresponding to an ideal zero pressure.

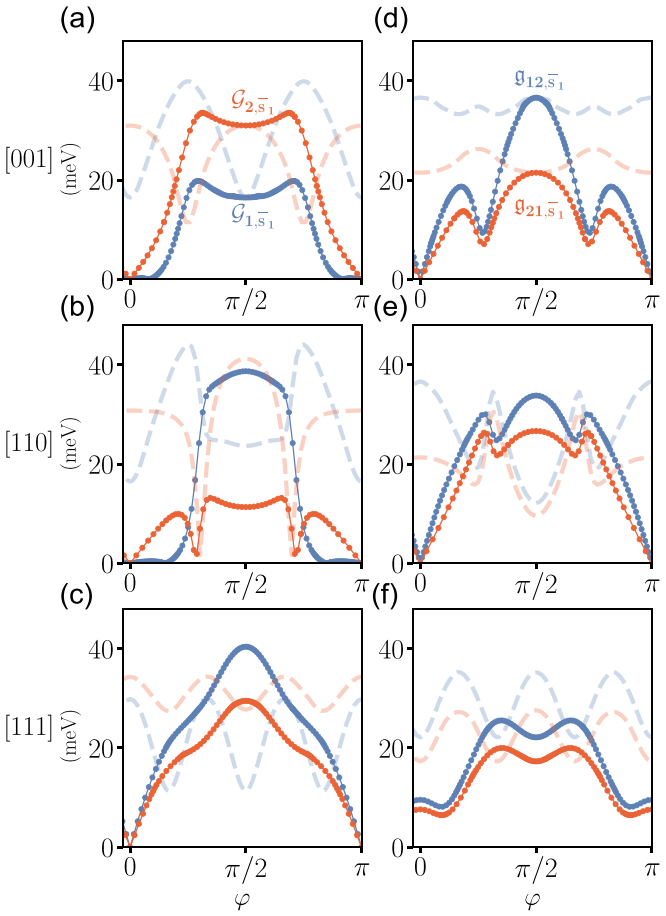

FIG. 11. Orientation dependence of the $\boldsymbol{q} = \boldsymbol{0}$ intraband (left) and interband (right) EPC for the $\bar{S}_1$ mode polarized in plane along k_1 for the three FS cuts, labeled on the left (E_{F1}; see Fig. 1). The in-plane polarizations of the mode are along (a) and (d) $k_1 = [100]$, (b) and (e) $k_1 = [001]$, and (c) and (f) $k_1 = [1\bar{1}0]$. φ is the azimuthal angle along the Fermi surface cut. Dashed lines are the EPC results for the perpendicular polarization in Fig. 3, shown here for comparison.

We used fully relativistic (scalar relativistic) projector augmented wave (PAW) method pseudopotentials for calculations with SOC (without SOC) [93] and the generalized gradient approximation for the exchange and correlation functional (Perdew-Burke-Ernzerhof) [94]. Convergence thresholds on total energy and forces were taken, respectively, as 5×10^{-6} and 10^{-5}. Cutoffs on wavefunctions and charge densities were, respectively, 55 and 550 Ry. Convergence threshold for self-consistency of electrons was 10^{-12}, with a maximum number of iterations for step 80 and mixing factor 0.4. The threshold for self-consistency in the phonon computation was 10^{-14}.

For electron-phonon calculations, we used an in-house-modified version of QE, which allows for the evaluation of Eq. (17) for any choice of the phonon eigenvector. In particular, we print the electron-phonon on the Cartesian basis set, i.e., $\gamma^{\kappa\alpha}_{nm}(\boldsymbol{k}, \boldsymbol{q})$ of Eq. (27). This is obtained by linking the displacements of each irreducible representation to the Cartesian one. These tasks are all performed by the `ph.x` program, which first performs the standard DFPT calculation of the linear response and, after convergence prints the electron-phonon. The contraction of the $\gamma^{\kappa\alpha}_{nm}(\boldsymbol{k}, \boldsymbol{q})$ matrices with any given phonon eigenvector is then easily performed in postprocessing.

2. Eigenfrequencies and eigenmodes

Decomposing the eigenvectors $\boldsymbol{e}^{\lambda}_{\kappa}(q = 0)$ computed by QE in the basis $(\bar{S}_1, \bar{S}_2, \bar{S}_3, \bar{S}_4)$, we get the following coefficients:

$$
\begin{aligned}
T_{1u}: &\ (0.966, 0.034, 0, 0) && (4.2\,\text{meV}),\\
T_{1u}: &\ (0.034, 0.965, 0, 0) && (22.7\,\text{meV}),\\
T_{1u}: &\ (0, 0, 1, 0) && (63.5\,\text{meV}),\\
T_{2u}: &\ (0, 0, 0, 1) && (32.3\,\text{meV}),
\end{aligned}
$$

where we have also added their corresponding frequency in millielectronvolts.

The eigenvectors and frequencies of the TO phonons determined by hyper-Raman scattering experiments at room temperature are [73]:

$$
\begin{aligned}
T_{1u}: &\ (0.991, 0.012, 0.0027, 0) && (10.0\ \text{meV}),\\
T_{1u}: &\ (0.011, 0.994, 0, 0) && (24.7\ \text{meV}),\\
T_{1u}: &\ (0.002, 0, 0.998, 0) && (67.7\ \text{meV}),\\
T_{2u}: &\ (0, 0, 0, 1) && (34.6\ \text{meV}).
\end{aligned}
$$

Therefore, the phonon spectra at the zone center computed by DFPT give results very similar to the experimentally reported eigenvectors (nearly pure $\bar{S}_\lambda$ modes) and frequencies. When computing Eq. (27), we used the experimental frequencies in Ref. [73] except for the soft TO mode, which has a strong temperature dependence, and we used instead its low temperature experimental frequency 2.5 meV, reported in Refs. [53,68].

3. Check against frozen-phonon calculations

The intraband DFPT results match the EPC obtained by a frozen-phonon method [41,56]. For that, we compute the relativistic electronic band splitting $\delta E_n(\boldsymbol{k})$ in the presence of a polar distortion $\bar{S}_\lambda$ with amplitude u, which gives the following EPC:

$$
\mathcal{G}^{\text{fr.ph.}}_{n,\lambda}(\boldsymbol{k}) = \frac{\delta E_{n,\lambda}(\boldsymbol{k})}{2u}\sqrt{\frac{\hbar}{2\mu_\lambda \omega_0}}. \tag{B1}
$$

The result is in agreement with degenerate perturbation theory to first order in u; i.e., interband processes can only

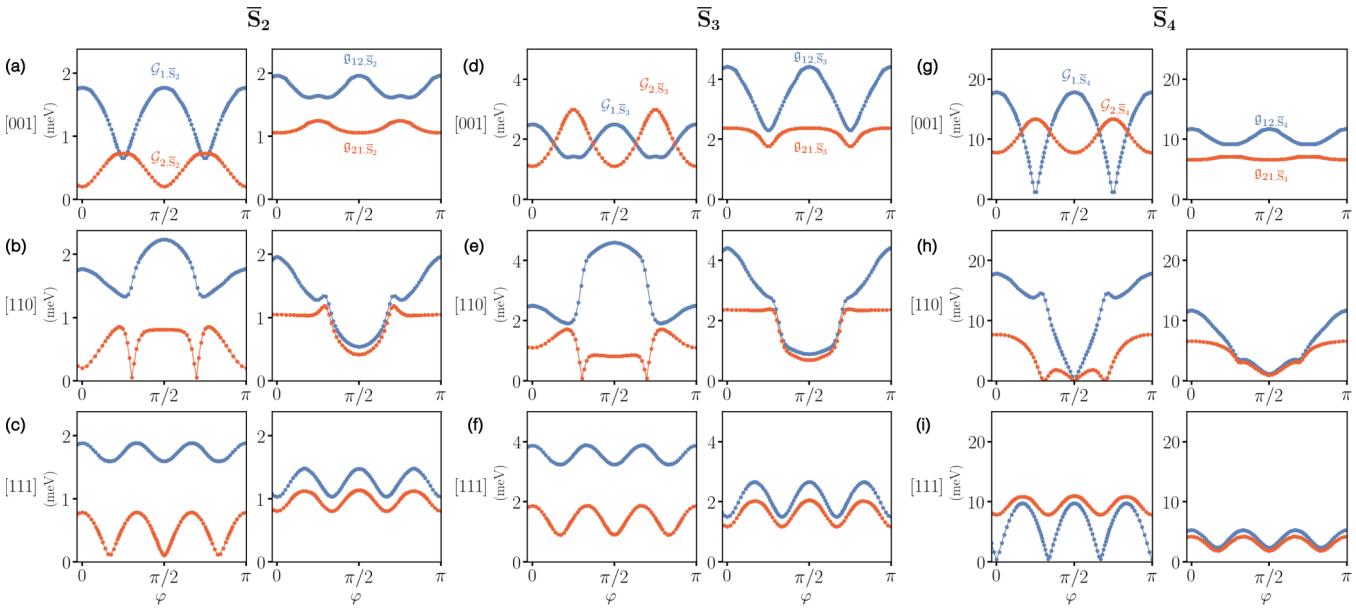

FIG. 12. Orientation dependence of the $\boldsymbol{q} = \boldsymbol{0}$ intraband and interband EPC for the following modes polarized perpendicular to the surface examined: (a)–(c) $\bar{S}_2$, (d)–(f) $\bar{S}_3$, and (g)–(i) $\bar{S}_4$. Panels are labeled on the left by the polarization of the mode. The EPC is evaluated on the Fermi surface with $E_{F,1} = 40$ meV. φ is the azimuthal angle along the Fermi surface cut. We used the experimental values for the frequency $\omega_{\boldsymbol{q}=0,\lambda} = 24.7, 67.7, 34.6$ meV, respectively [68].

affect higher order in u quantities, not the breaking of the degeneracy. Hence, to linear order in u, the EPC obtained from DFPT and frozen phonon is formally exact, and we find this to be respected up to a precision of $0.005 \div 0.05$ meV (root mean square of $\lesssim 0.01$ meV) for displacements of $u = 0.001$ Å.

4. Phonon with in-plane polarization

As shown in Fig. 11 with the full lines, also for a polarization vector parallel to the FS cut, the three orientations have comparable EPC with the $\bar{S}_1$ mode. Furthermore, the azimuthal dependence is such that matrix elements are overall smaller than for the mode polarized normal to the cut (dashed lines). For example, for the [001] orientation, in Figs. 11(a) and 11(d), the coupling is constrained to be equal to the normal polarization at $\varphi = \pi/2$ and then approaches zero at $\varphi = 0, \pi$ (while the normal polarization case stays finite). For the other directions, one finds a similar behavior.

5. Orientation dependence for optical modes

We show for completeness our DFPT results for modes $\bar{S}_2$, $\bar{S}_3$, and $\bar{S}_4$ in Fig. 12 for FS cuts at $E_{F,1} = 40$ meV perpendicular to the three orientations [001], [110], and [111]. The strength of the EPC has a strong azimuthal angular dependence in all cases, as seen for the $\bar{S}_1$ mode (Fig. 3). Similar to the soft mode, the strength observed along the three FS cuts is comparable in all modes, making it difficult to claim anything from our calculations about the orientation dependence of T_c. As we underline in our conclusions, however, in the weak coupling regime, small differences are strongly enhanced by the exponential dependence. A detailed computation of T_c goes beyond the scope of this work and is left for future investigations.

[1] J. H. Barrett, Dielectric constant in perovskite type crystals, Phys. Rev. **86**, 118 (1952).

[2] S. H. Wemple, Some transport properties of oxygen-deficient single-crystal potassium tantalate ($KTaO_3$), Phys. Rev. **137**, A1575 (1965).

[3] R. A. Cowley, Lattice dynamics and phase transitions of strontium titanate, Phys. Rev. **134**, A981 (1964).

[4] J. D. Axe, J. Harada, and G. Shirane, Anomalous acoustic dispersion in centrosymmetric crystals with soft optic phonons, Phys. Rev. B **1**, 1227 (1970).

[5] R. Migoni, H. Bilz, and D. Bäuerle, Origin of Raman scattering and ferroelectricity in oxidic perovskites, Phys. Rev. Lett. **37**, 1155 (1976).

[6] K. A. Müller and H. Burkard, $SrTiO_3$: An intrinsic quantum paraelectric below 4 K, Phys. Rev. B **19**, 3593 (1979).

[7] S. Rowley, L. Spalek, R. Smith, M. Dean, M. Itoh, J. Scott, G. Lonzarich, and S. Saxena, Ferroelectric quantum criticality, Nat. Phys. **10**, 367 (2014).

[8] G. G. Guzmán-Verri, C. H. Liang, and P. B. Littlewood, Lamellar fluctuations melt ferroelectricity, Phys. Rev. Lett. **131**, 046801 (2023).

[9] X. Lin, Z. Zhu, B. Fauqué, and K. Behnia, Fermi surface of the most dilute superconductor, Phys. Rev. X **3**, 021002 (2013).

[10] C. S. Koonce, M. L. Cohen, J. F. Schooley, W. R. Hosler, and E. R. Pfeiffer, Superconducting transition temperatures of semiconducting $SrTiO_3$, Phys. Rev. **163**, 380 (1967).

[11] M. N. Gastiasoro, J. Ruhman, and R. M. Fernandes, Superconductivity in dilute $SrTiO_3$: A review, Ann. Phys. (NY) **417**, 168107 (2020).

[12] A. D. Caviglia, S. Gariglio, N. Reyren, D. Jaccard, T. Schneider, M. Gabay, S. Thiel, G. Hammerl, J. Mannhart, and J. M. Triscone, Electric field control of the $LaAlO_3/SrTiO_3$ interface ground state, Nature (London) **456**, 624 (2008).

[13] Y.-Y. Pai, A. Tylan-Tyler, P. Irvin, and J. Levy, Physics of $SrTiO_3$-based heterostructures and nanostructures: A review, Rep. Prog. Phys. **81**, 036503 (2018).

[14] K. Ueno, S. Nakamura, H. Shimotani, H. Yuan, N. Kimura, T. Nojima, H. Aoki, Y. Iwasa, and M. Kawasaki, Discovery of superconductivity in $KTaO_3$ by electrostatic carrier doping, Nat. Nanotechnol. **6**, 408 (2011).

[15] C. Liu, X. Yan, D. Jin, Y. Ma, H.-W. Hsiao, Y. Lin, T. M. Bretz-Sullivan, X. Zhou, J. Pearson, B. Fisher, *et al.*, Two-dimensional superconductivity and anisotropic transport at $KTaO_3$ (111) interfaces, Science **371**, 716 (2021).

[16] Z. Chen, Z. Liu, Y. Sun, X. Chen, Y. Liu, H. Zhang, H. Li, M. Zhang, S. Hong, T. Ren, C. Zhang, H. Tian, Y. Zhou, J. Sun, and Y. Xie, Two-dimensional superconductivity at the $LaAlO_3/KTaO_3$ (110) heterointerface, Phys. Rev. Lett. **126**, 026802 (2021).

[17] Z. Chen, Y. Liu, H. Zhang, Z. Liu, H. Tian, Y. Sun, M. Zhang, Y. Zhou, J. Sun, and Y. Xie, Electric field control of superconductivity at the $LaAlO_3/KTaO_3$ (111) interface, Science **372**, 721 (2021).

[18] T. Ren, M. Li, X. Sun, L. Ju, Y. Liu, S. Hong, Y. Sun, Q. Tao, Y. Zhou, Z.-A. Xu, *et al.*, Two-dimensional superconductivity at the surfaces of $KTaO_3$ gated with ionic liquid, Sci. Adv. **8**, eabn4273 (2022).

[19] C. Liu, X. Zhou, D. Hong, B. Fisher, H. Zheng, J. Pearson, J. S. Jiang, D. Jin, M. R. Norman, and A. Bhattacharya, Tunable superconductivity and its origin at $KTaO_3$ interfaces, Nat. Commun. **14**, 951 (2023).

[20] S. Mallik, G. Ménard, G. Saïz, H. Witt, J. Lesueur, A. Gloter, L. Benfatto, M. Bibes, and N. Bergeal, Superfluid stiffness of a $KTaO_3$-based two-dimensional electron gas, Nat. Commun. **13**, 4625 (2022).

[21] D. Maryenko, I. V. Maznichenko, S. Ostanin, M. Kawamura, K. S. Takahashi, M. Nakamura, V. K. Dugaev, E. Y. Sherman, A. Ernst, and M. Kawasaki, Superconductivity at epitaxial $LaTiO_3$–$KTaO_3$ interfaces, APL Mater. **11**, 061102 (2023).

[22] X. Chen, T. Yu, Y. Liu, Y. Sun, M. Lei, N. Guo, Y. Fan, X. Sun, M. Zhang, F. Alarab, *et al.*, Orientation-dependent electronic structure in interfacial superconductors $LaAlO_3/KTaO_3$, Nat. Commun. **15**, 7704 (2024).

[23] J. M. Edge, Y. Kedem, U. Aschauer, N. A. Spaldin, and A. V. Balatsky, Quantum critical origin of the superconducting dome in $SrTiO_3$, Phys. Rev. Lett. **115**, 247002 (2015).

[24] P. Wölfle and A. V. Balatsky, Superconductivity at low density near a ferroelectric quantum critical point: Doped $SrTiO_3$, Phys. Rev. B **98**, 104505 (2018).

[25] V. Kozii, Z. Bi, and J. Ruhman, Superconductivity near a ferroelectric quantum critical point in ultralow-density Dirac materials, Phys. Rev. X **9**, 031046 (2019).

[26] M. N. Gastiasoro, T. V. Trevisan, and R. M. Fernandes, Anisotropic superconductivity mediated by ferroelectric fluctuations in cubic systems with spin-orbit coupling, Phys. Rev. B **101**, 174501 (2020).

[27] C. Setty, M. Baggioli, and A. Zaccone, Superconducting dome in ferroelectric-type materials from soft mode instability, Phys. Rev. B **105**, L020506 (2022).

[28] C. W. Rischau, X. Lin, C. P. Grams, D. Finck, S. Harms, J. Engelmayer, T. Lorenz, Y. Gallais, B. Fauque, J. Hemberger, *et al.*, A ferroelectric quantum phase transition inside the superconducting dome of $Sr_{1-x}Ca_xTiO_{3-\delta}$, Nat. Phys. **13**, 643 (2017).

[29] C. W. Rischau, D. Pulmannová, G. W. Scheerer, A. Stucky, E. Giannini, and D. van der Marel, Isotope tuning of the superconducting dome of strontium titanate, Phys. Rev. Res. **4**, 013019 (2022).

[30] Y. Tomioka, N. Shirakawa, and I. H. Inoue, Superconductivity enhancement in polar metal regions of $Sr_{0.95}Ba_{0.05}TiO_3$ and $Sr_{0.985}Ca_{0.015}TiO_3$ revealed by systematic Nb doping, npj Quantum Mater. **7**, 111 (2022).

[31] S. Hameed, D. Pelc, Z. W. Anderson, A. Klein, R. Spieker, L. Yue, B. Das, J. Ramberger, M. Lukas, Y. Liu, *et al.*, Enhanced superconductivity and ferroelectric quantum criticality in plastically deformed strontium titanate, Nat. Mater. **21**, 54 (2022).

[32] S. K. Saha, M. N. Gastiasoro, J. Ruhman, and A. Klein, Strong coupling theory of superconductivity and ferroelectric quantum criticality in metallic $SrTiO_3$, npj Quantum Mater. **10**, 82 (2025).

[33] J. Ruhman and P. A. Lee, Comment on "superconductivity at low density near a ferroelectric quantum critical point: Doped $SrTiO_3$", Phys. Rev. B **100**, 226501 (2019).

[34] K. L. Ngai, Two-phonon deformation potential and superconductivity in degenerate semiconductors, Phys. Rev. Lett. **32**, 215 (1974).

[35] D. van der Marel, F. Barantani, and C. W. Rischau, Possible mechanism for superconductivity in doped $SrTiO_3$, Phys. Rev. Res. **1**, 013003 (2019).

[36] D. E. Kiselov and M. V. Feigel'man, Theory of superconductivity due to Ngai's mechanism in lightly doped $SrTiO_3$, Phys. Rev. B **104**, L220506 (2021).

[37] P. A. Volkov, P. Chandra, and P. Coleman, Superconductivity from energy fluctuations in dilute quantum critical polar metals, Nat. Commun. **13**, 4599 (2022).

[38] V. Kozii and L. Fu, Odd-parity superconductivity in the vicinity of inversion symmetry breaking in spin-orbit-coupled systems, Phys. Rev. Lett. **115**, 207002 (2015).

[39] M. N. Gastiasoro, M. E. Temperini, P. Barone, and J. Lorenzana, Theory of superconductivity mediated by Rashba coupling in incipient ferroelectrics, Phys. Rev. B **105**, 224503 (2022).

[40] Y. Yu, H. Y. Hwang, S. Raghu, and S. B. Chung, Theory of superconductivity in doped quantum paraelectrics, npj Quantum Mater. **7**, 63 (2022).

[41] M. N. Gastiasoro, M. E. Temperini, P. Barone, and J. Lorenzana, Generalized Rashba electron-phonon coupling and superconductivity in strontium titanate, Phys. Rev. Res. **5**, 023177 (2023).

[42] A. Klein, V. Kozii, J. Ruhman, and R. M. Fernandes, Theory of criticality for quantum ferroelectric metals, Phys. Rev. B **107**, 165110 (2023).

[43] A. Kumar, P. Chandra, and P. A. Volkov, Phonon-induced collective modes in spin-orbit coupled polar metals, Phys. Rev. B **108**, 075162 (2023).

[44] M. Schlipf and F. Giustino, Dynamic Rashba-Dresselhaus effect, Phys. Rev. Lett. **127**, 237601 (2021).

[45] L. Chen, S. Zhou, D. Tian, Y. Xiao, Q. Gao, Y. Wang, Y. Chen, F. Hu, B. Shen, J. Sun, W. Zhao, J. Zhang, and H. Zhang, Two-dimensional superconductivity at the $CaZrO_3/KTaO_3$ (001) heterointerfaces, arXiv:2507.01392.

[46] L. F. Mattheiss, Energy bands for $KNiF_3$, $SrTiO_3$, $KMoO_3$, and $KTaO_3$, Phys. Rev. B **6**, 4718 (1972).

[47] H. Uwe, K. Oka, H. Unoki, and T. Sakudo, Raman scattering from conduction electron in $KTaO_3$, J. Phys. Soc. Jpn. **49**, 577 (1980).

[48] E. G. Arnault, A. H. Al-Tawhid, S. Salmani-Rezaie, D. A. Muller, D. P. Kumah, M. S. Bahramy, G. Finkelstein, and K. Ahadi, Anisotropic superconductivity at $KTaO_3$(111) interfaces, Sci. Adv. **9**, eadf1414 (2023).

[49] A. H. Al-Tawhid, S. J. Poage, S. Salmani-Rezaie, A. Gonzalez, S. Chikara, D. A. Muller, D. P. Kumah, M. N. Gastiasoro, J. Lorenzana, and K. Ahadi, Enhanced critical field of superconductivity at an oxide interface, Nano Lett. **23**, 6944 (2023).

[50] U. Filippozzi, G. Kimbell, D. Pizzirani, S. M. Walker, C. Cocchi, S. Gariglio, M. Gabay, S. Wiedmann, and A. D. Caviglia, High-field superconductivity from atomic-scale confinement and spin-orbit coupling at (111) $LaAlO_3/KTaO_3$ interfaces, arXiv:2411.05668.

[51] S. J. Poage, X. Gao, M. Baksi, S. Salmani-Rezaie, D. A. Muller, D. P. Kumah, C. N. Lau, J. Lorenzana, M. N. Gastiasoro, and K. Ahadi, Violation of the Pauli limit at $KTaO_3$(110) interfaces, Phys. Rev. B **111**, 214506 (2025).

[52] J. Yang, C. Liu, X. Zhou, H. Hou, K. Yin, J. Wen, J. Pearson, A. Suslov, D. Jin, J. S. Jiang, U. Welp, J.-M. Zuo, M. R. Norman, and A. Bhattacharya, Uniaxial spin texture in a superconducting electron gas revealed by exchange interactions, arXiv:2502.19599.

[53] Z. Chu, J. Yang, Y. Li, K. Hwangbo, J. Wen, A. R. Bielinski, Q. Zhang, A. B. F. Martinson, S. O. Hruszkewycz, D. D. Fong, X. Xu, M. R. Norman, A. Bhattacharya, and H. Wen, Revealing subterahertz atomic vibrations in quantum paraelectrics by surface-sensitive spintronic terahertz spectroscopy, Sci. Adv. **10**, eads8601 (2024).

[54] F. Macheda, P. Barone, and F. Mauri, Electron-phonon interaction and longitudinal-transverse phonon splitting in doped semiconductors, Phys. Rev. Lett. **129**, 185902 (2022).

[55] T. Esswein and N. A. Spaldin, First-principles calculation of electron-phonon coupling in doped $KTaO_3$, Open Res. Eur. **3**, 177 (2023).

[56] G. Venditti, M. E. Temperini, P. Barone, J. Lorenzana, and M. N. Gastiasoro, Anisotropic Rashba coupling to polar modes in $KTaO_3$, J. Phys.: Mater. **6**, 014007 (2023).

[57] F. Y. Bruno, S. McKeown Walker, S. Riccò, A. De La Torre, Z. Wang, A. Tamai, T. K. Kim, M. Hoesch, M. S. Bahramy, and F. Baumberger, Band structure and spin–orbital texture of the (111)-$KTaO_3$ 2D electron gas, Adv. Electron. Mater. **5**, 1800860 (2019).

[58] G. L. Stamokostas and G. A. Fiete, Mixing of $t_{2g} - e_g$ orbitals in 4*d* and 5*d* transition metal oxides, Phys. Rev. B **97**, 085150 (2018).

[59] D. I. Khomskii and S. V. Streltsov, Orbital effects in solids: Basics, recent progress, and opportunities, Chem. Rev. **121**, 2992 (2021).

[60] E. I. Blount, Symmetry properties of triplet superconductors, Phys. Rev. B **32**, 2935 (1985).

[61] L. Fu, Parity-breaking phases of spin-orbit-coupled metals with gyrotropic, ferroelectric, and multipolar orders, Phys. Rev. Lett. **115**, 026401 (2015).

[62] S. Kanasugi and Y. Yanase, Spin-orbit-coupled ferroelectric superconductivity, Phys. Rev. B **98**, 024521 (2018).

[63] P. A. Volkov and P. Chandra, Multiband quantum criticality of polar metals, Phys. Rev. Lett. **124**, 237601 (2020).

[64] S. Sumita and Y. Yanase, Superconductivity induced by fluctuations of momentum-based multipoles, Phys. Rev. Res. **2**, 033225 (2020).

[65] J. M. Luttinger, Quantum theory of cyclotron resonance in semiconductors: General theory, Phys. Rev. **102**, 1030 (1956).

[66] L. Savary, J. Ruhman, J. W. F. Venderbos, L. Fu, and P. A. Lee, Superconductivity in three-dimensional spin-orbit coupled semimetals, Phys. Rev. B **96**, 214514 (2017).

[67] W. Kohn, Nobel lecture: Electronic structure of matter—wave functions and density functionals, Rev. Mod. Phys. **71**, 1253 (1999).

[68] H. Vogt, Refined treatment of the model of linearly coupled anharmonic oscillators and its application to the temperature dependence of the zone-center soft-mode frequencies of $KTaO_3$ and $SrTiO_3$, Phys. Rev. B **51**, 8046 (1995).

[69] X. He, D. Bansal, B. Winn, S. Chi, L. Boatner, and O. Delaire, Anharmonic eigenvectors and acoustic phonon disappearance in quantum paraelectric $SrTiO_3$, Phys. Rev. Lett. **124**, 145901 (2020).

[70] L. Ranalli, C. Verdi, L. Monacelli, G. Kresse, M. Calandra, and C. Franchini, Temperature-dependent anharmonic phonons in quantum paraelectric $KTaO_3$ by first principles and machine-learned force fields, Adv. Quantum Technol. **6**, 2200131 (2023).

[71] J. D. Axe, Apparent ionic charges and vibrational eigenmodes of $BaTiO_3$ and other perovskites, Phys. Rev. **157**, 429 (1967).

[72] J. Harada, J. Axe, and G. Shirane, Determination of the normal vibrational displacements in several perovskites by inelastic neutron scattering, Acta Crystallogr. Sect. A **26**, 608 (1970).

[73] H. Vogt, Hyper-Raman tensors of the zone-center optical phonons in $SrTiO_3$ and $KTaO_3$, Phys. Rev. B **38**, 5699 (1988).

[74] A. F. Santander-Syro, C. Bareille, F. Fortuna, O. Copie, M. Gabay, F. Bertran, A. Taleb-Ibrahimi, P. Le Fèvre, G. Herranz, N. Reyren, M. Bibes, A. Barthélémy, P. Lecoeur, J. Guevara, and M. J. Rozenberg, Orbital symmetry reconstruction and strong mass renormalization in the two-dimensional electron gas at the surface of $KTaO_3$, Phys. Rev. B **86**, 121107(R) (2012).

[75] S. Mallik, B. Göbel, H. Witt, L. M. Vicente-Arche, S. Varotto, J. Bréhin, G. Ménard, G. Saïz, D. Tamsaout, A. F. Santander-Syro, F. Fortuna, F. Bertran, P. Le Fèvre, J. Rault, I. Boventer, I. Mertig, A. Barthélémy, N. Bergeal, A. Johansson, and M. Bibes, Electronic band structure of superconducting $KTaO_3$ (111) interfaces, APL Mater. **11**, 121108 (2023).

[76] K. Rubi, S. Zeng, F. Bangma, M. Goiran, A. Ariando, W. Escoffier, and U. Zeitler, Electronic subbands in the *a*-$LaAlO_3/KTaO_3$ interface revealed by quantum oscillations in high magnetic fields, Phys. Rev. Res. **3**, 033234 (2021).

[77] K. Rubi, D. R. Candido, M. Dumen, S. Zeng, E. L. Q. N. Ammerlaan, F. Bangma, M. K. Chan, M. Goiran, A. Ariando, S. Chakraverty, W. Escoffier, U. Zeitler, and N. Harrison, Unconventional quantum oscillations and evidence of nonparabolic electronic states in quasi-two-dimensional electron system at complex oxide interfaces, Phys. Rev. Res. **6**, 043231 (2024).

[78] F. Macheda, T. Sohier, P. Barone, and F. Mauri, Electron-phonon interaction and phonon frequencies in two-dimensional doped semiconductors, Phys. Rev. B **107**, 094308 (2023).

[79] F. Macheda, P. Barone, and F. Mauri, First-principles calculations of dynamical Born effective charges, quadrupoles, and higher order terms from the charge response in large semiconducting and metallic systems, Phys. Rev. B **110**, 094306 (2024).

[80] N. Marzari, A. A. Mostofi, J. R. Yates, I. Souza, and D. Vanderbilt, Maximally localized Wannier functions: Theory and applications, Rev. Mod. Phys. **84**, 1419 (2012).

[81] G. Chaudhary and I. Martin, Superconductivity from polar fluctuations in multi-orbital systems, arXiv:2306.11063.

[82] W. Zhou, R. Guzman, M. Pruneda, J. P. Nery, M. Xu, A. Li, N. Wittemeier, A. Li, G. Singh, N. Bergeal, *et al.*, Electron-phonon coupling and symmetry-breaking in superconducting oxide interfaces near ferroelectric quantum criticality, preprint Research Square, available at: https://doi.org/10.21203/rs.3.rs-6991826/v1.

[83] M. N. Gastiasoro, G. Venditti, and F. Macheda, Data for article 'Spin-dependent anisotropic electron-phonon coupling in $KTaO_3$', Zenodo (2026), http://doi.org/10.5281/zenodo.17515838.

[84] A. A. Mostofi, J. R. Yates, G. Pizzi, Y.-S. Lee, I. Souza, D. Vanderbilt, and N. Marzari, An updated version of wannier90: A tool for obtaining maximally-localised Wannier functions, Comput. Phys. Commun. **185**, 2309 (2014).

[85] K. V. Shanavas and S. Satpathy, Electric field tuning of the Rashba effect in the polar perovskite structures, Phys. Rev. Lett. **112**, 086802 (2014).

[86] K. V. Shanavas, Z. S. Popović, and S. Satpathy, Theoretical model for Rashba spin-orbit interaction in *d* electrons, Phys. Rev. B **90**, 165108 (2014).

[87] K. V. Shanavas, Theoretical study of the cubic Rashba effect at the $SrTiO_3$(001) surfaces, Phys. Rev. B **93**, 045108 (2016).

[88] M. Kim, J. Ihm, and S. B. Chung, Strongly enhanced rashba splittings in an oxide heterostructure: A tantalate monolayer on $BaHfO_3$, Phys. Rev. B **94**, 115431 (2016).

[89] M. Lee, H.-J. Lee, J. H. Lee, and S. B. Chung, Topological superconductivity from transverse optical phonons in oxide heterostructures, Phys. Rev. Mater. **4**, 034202 (2020).

[90] H. Djani, A. C. Garcia-Castro, W.-Y. Tong, P. Barone, E. Bousquet, S. Picozzi, and P. Ghosez, Rationalizing and engineering Rashba spin-splitting in ferroelectric oxides, npj Quantum Mater. **4**, 51 (2019).

[91] F. Birch, Finite elastic strain of cubic crystals, Phys. Rev. **71**, 809 (1947).

[92] P. Vousden, A study of the unit-cell dimensions and symmetry of certain ferroelectric compounds of niobium and tantalum at room temperature, Acta Crystallogr. **4**, 373 (1951).

[93] A. Dal Corso, Pseudopotentials periodic table: From H to Pu, Comput. Mater. Sci. **95**, 337 (2014).

[94] J. P. Perdew, K. Burke, and M. Ernzerhof, Generalized gradient approximation made simple, Phys. Rev. Lett. **77**, 3865 (1996).